Journal of Sound and Vibration 649 (2027) 120226

Contents lists available at ScienceDirect

Journal of Sound and Vibration

journal homepage: www.elsevier.com/locate/jsvi

Wake characteristics induced by bending oscillation of a cantilevered needle in confined planar channel flow

Ziman Wang [a], Tong Liang [a], Changzhao Jiang [b,*], Yuanhao Yin [c], Xiaohu Gu [a], Heping Xiang [a], Yingjie Chen [d], Yan Cao [e]

[a] School of Mechanical Engineering, Beijing Institute of Technology, Beijing 100081, China
[b] Mechanical and Aerospace Engineering department, Brunel University London, London, England, UK
[c] Beijing institute of aerospace testing technology, Beijing 100074, China
[d] Nanyue Electric Control Co., LTD, Hengyang 421000, China
[e] Shanxi Diesel Engine Industry Co., LTD, Datong 037001, China

ARTICLE INFO

Keywords:
Needle oscillation
Wake transition
Reverse-Kármán-type wake
Hydrodynamic damping

ABSTRACT

Understanding the wake dynamics of oscillating fuel-injector needles is critical for optimizing injection performance. To isolate the underlying mechanisms, this study employs an idealized two-dimensional model of a cantilever needle oscillating in planar channel flow. The effects of oscillation parameters, inflow velocity, fluid properties, needle-tip geometry, and bending mode on wake dynamics are systematically investigated, together with the resulting hydrodynamic forces and damping. Increasing oscillation intensity enhances near-tip vorticity and promotes asymmetric shear-layer roll-up, driving the wake from a Kármán-type to a reverse-Kármán-type pattern, whereas increasing inflow velocity or viscosity favors the opposite transition. The combined effects are characterized by the modified Strouhal number (St_A) and Reynolds number (Re), with a power-law transition boundary identified in the St_A-Re regime map. The transverse hydrodynamic damping changes from positive to negative as inflow velocity increases, indicating a reversal in fluid-structure energy transfer from energy dissipation to energy input. Variations in tip geometry and bending mode do not fundamentally alter the wake mechanism. These findings provide a mechanistic basis for understanding oscillation-induced wake dynamics, and may inform future assessment and optimization of vibration and flow stability in fuel-injector systems.

1. Introduction

In many closed-type fuel injectors, including those operating with diesel, methanol, and liquid ammonia, high-pressure transient flow can induce high-frequency bending vibrations of the internal needle, as shown in Fig. 1(a). Such needle oscillation can substantially disturb the surrounding flow field and may influence the flow delivered to the nozzle orifices, thereby affecting injection consistency, spray development, and ultimately engine performance. Therefore, investigating the oscillation characteristics of the needle is of great significance for optimizing fuel injector performance, mitigating harmful vibrations, and reducing flow nonuniformity among nozzle orifices. To isolate the associated flow mechanisms, the needle was idealized as a two-dimensional (2D) cantilever beam clamped at its upper end and prescribed to undergo harmonic bending oscillation, with the maximum displacement

* Corresponding author.
E-mail address: changzhao.jiang@brunel.ac.uk (C. Jiang).

https://doi.org/10.1016/j.jsv.2026.120226
Received 30 March 2026; Received in revised form 28 October 2026; Accepted 30 October 2026
Available online 31 October 2026
0022-460X/© 2026 The Authors. Published by Elsevier Ltd. This is an open access article under the CC BY license (http://creativecommons.org/licenses/by/4.0/).

occurring at the free tip (Fig. 1(b)).

Previous studies have investigated injector needle motion using both experimental and numerical approaches. X-ray phase-contrast imaging has been employed to directly observe needle motion and identify characteristic oscillation patterns [1]. To visualize internal flow structures, transparent nozzles are employed to examine cavitation dynamics [2]. Numerically, needle displacement has commonly been represented through prescribed eccentricity in quasi-static calculations [2,3] or transverse rigid-body motion [4,5]. These studies have demonstrated that, in practical multi-hole injectors, needle motion can significantly alter the mass flow rates through individual orifices to different extents during the opening and closing phases, thereby leading to increased hole-to-hole flow nonuniformity and reduced injection consistency [4,5]. However, most investigations have focused on macroscopic needle motion [1], cavitation [2], or overall injection characteristics, whereas the detailed wake generated by high-frequency lateral oscillation and its relation to unsteady hydrodynamic loading remain comparatively less understood. In addition, rigid-body representations cannot reproduce the spatially varying displacement associated with bending deformation of a cantilevered needle [6].

Beyond injector-specific studies, reduced-order and finite-element models have been widely used to investigate nonlinear flow-induced oscillations, capturing the coupled effects of unsteady fluid loading, structural deformation, and stability [7–10]. These studies provide a useful modeling basis for idealizing the oscillatory response of slender cantilevered structures. The aforementioned common modeling methods are illustrated in Fig. 2.

A broad range of computational frameworks has been developed for oscillating-body fluid-structure interaction, including reduced-order vortex methods, unsteady vortex-lattice formulations, and coupled Navier-Stokes/structural solvers. These studies have demonstrated that wake dynamics, fluid loading, and the resulting structural response can depend strongly on structural compliance, oscillator arrangement, separation modeling, and the phase relationship between body motion and fluid force [7,11–16].

For an oscillating injector needle, such fluid-structure interactions are closely linked to the surrounding wake dynamics and the resulting unsteady hydrodynamic loads [17]. The wake is particularly relevant because oscillatory motion can reorganize the shear layers around the needle and generate alternating vortical structures, which in turn produce unsteady pressure and hydrodynamic forces. Moreover, in practical multi-hole injectors, needle-induced vortical structures may interact with the sac flow and alter the local inflow conditions at individual nozzle-hole inlets, potentially contributing to hole-to-hole flow nonuniformity [18,19].

Beginning with the classical Kármán vortex street [20], experiments and numerical studies have reported transitions of the primary wake toward secondary vortex structures [21–26]. The first transition appears in the near wake, evolving from the main vortex street into a two-layered vortex street. The second transition occurs in the far wake, shifting from the two-layered structure to the secondary vortex street.

These transitions have been attributed to mechanisms including hydrodynamic instability and vortex merging [24–30], with their occurrence and downstream location exhibiting a pronounced dependence on the Reynolds number. Such studies demonstrate the sensitivity of vortex organization to both viscous effects and flow conditions, but they primarily concern stationary or conventionally

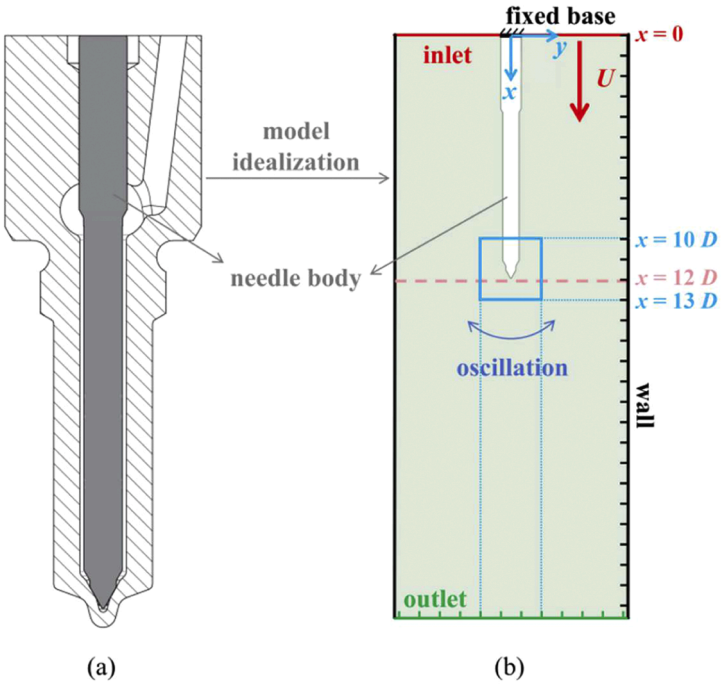


Fig. 1. From real injector configuration to idealized cantilevered needle model: (a) injector cross-section; (b) idealized 2D cantilevered needle model for wake analysis. The needle body itself is modeled as a cantilever structure, whose upper end is fixed to a rigid support. Here, D denotes the characteristic diameter of the needle, while $x = 10D$, $12D$, and $13D$ indicate the corresponding streamwise locations measured from the inlet.

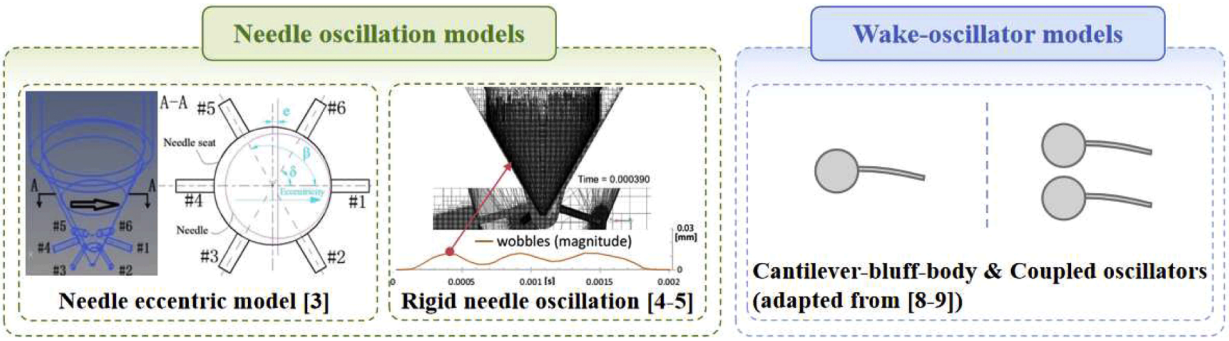


Fig. 2. Modeling approaches used in previous studies of fuel-injector needle oscillation and reduced-order models for flow-induced vibration.

forced bluff bodies rather than bending-oscillating injector needles.

Periodic transverse forcing can further reorganize a conventional Kármán-type wake into an oppositely arranged, reverse-Kármán-type wake. For oscillating or flapping foils, Godoy-Diana [31] and He et al. [32] showed that, at constant Re and Strouhal number (St), an increase in the amplitude-to-chord ratio causes the wake to transition from a Kármán-type wake through an aligned alternating-vortex wake (2S mode [33]) toward a reverse-Kármán-type wake. The corresponding wake reorganization is also closely associated with changes in the hydrodynamic forces acting on the oscillating body [31]. Dynnikova [34] further demonstrated that wake morphology is sensitive to angle amplitudes (α_0), while theoretical studies have linked the instability and symmetry breaking of the reverse-Kármán-type wake to bending disturbances [20,35]. These results establish oscillation amplitude, frequency, and flow conditions as key parameters controlling forced wakes.

Previous studies of flapping foils have further shown that a deflected reverse-Kármán wake may undergo quasi-periodic motion, intermittent switching, and eventually chaotic dynamics when the forcing is increased, and that near-field vortex interactions can propagate into a reorganization of the far wake [36]. Structural flexibility can substantially modify this sequence by regularizing the near-field interactions and restoring wake periodicity over an appropriate flexibility range, although excessive flexibility may again promote aperiodicity [11,12]. These findings indicate that wake topology alone does not uniquely characterize the long-time dynamical state.

Despite these extensive efforts, several issues remain unresolved for oscillating fuel-injector needles. First, most studies of Kármán- to reverse-Kármán-type wake transitions have been conducted for canonical bodies in water or air [31,34,37], whereas injector applications involve liquids whose density and viscosity may vary substantially with fuel type and operating condition. Previous studies have shown that fluid properties can affect needle oscillation behavior, with increased viscosity tending to suppress the vibration response [38,39]. However, how fluid density and viscosity interact with oscillation parameters and inflow velocity to determine the wake pattern has not been systematically established. In particular, a unified description capable of incorporating these effects into a wake-transition framework is still lacking. Second, although wake reorganization necessarily modifies the unsteady force acting on the needle, the associated force characteristics, fluid-structure energy transfer, and hydrodynamic damping have received limited attention. Finally, it remains unclear whether the fundamental wake response is sensitive to needle-tip geometry and bending-oscillation mode.

Accordingly, the present study employs an idealized 2D cantilevered-needle model to isolate the fundamental interaction between prescribed bending oscillation and the surrounding flow. The effects of oscillation amplitude, frequency, inflow velocity, and fluid properties on wake morphology and vortex dynamics are systematically examined. The combined influence of these parameters is characterized using the modified Strouhal number (St_A) and Reynolds number (Re) to establish a regime description of the transition between Kármán-type and reverse-Kármán-type wakes. The corresponding streamwise and transverse hydrodynamic forces are analyzed together with the transverse hydrodynamic damping to clarify the associated fluid-structure energy transfer. The sensitivities of the wake to needle-tip geometry and bending-oscillation mode are also assessed. In addition, a representative three-dimensional (3D) simulation is conducted to examine the influence of spanwise flow development and to clarify the limitations of the 2D approximation.

From a practical perspective, the model helps address the difficulty of identifying the specific contribution of needle vibration to near-tip wake reorganization in a highly coupled injector environment. The resulting wake characteristics and hydrodynamic responses provide a basis for identifying oscillation and flow conditions associated with enhanced wake asymmetry and unsteady hydrodynamic loading, thereby providing mechanistic insight for the assessment of injector flow stability and future fluid–structure interaction studies.

2. Numerical method and experiment setup

2.1. Numerical method

2.1.1. Governing equation

In this study, the temperature within the 2D flow field is assumed to remain constant, and surface tension effects are neglected. The fluid exhibits incompressible viscous behavior. To characterize the flow regime associated with the wake induced by the oscillating needle, the Reynolds number is introduced, defined as:

$$Re = \rho D U_0 / \mu \tag{1}$$

where U_0 is the inflow velocity, ρ is the density, μ is the dynamic viscosity, and D is the needle diameter ($D = 3.5$ mm). In the present study, the Reynolds number ranges from 62.8 to 1123.7. Therefore, the flow field around the oscillating cantilever needle is resolved using the laminar Navier-Stokes equations. The governing equations are expressed as follows:

(i) Continuity Equation

$$\nabla \cdot \mathbf{u} = 0 \tag{2}$$

(ii) Momentum Equations

$$\frac{\partial \mathbf{u}}{\partial t} + (\mathbf{u} \cdot \nabla)\mathbf{u} = -\frac{1}{\rho}\nabla p + \nu \nabla^2 \mathbf{u} \tag{3}$$

where $\mathbf{u}$ is the velocity field (u_x, u_y), t is time, and $\nu = \mu/\rho$ is the kinematic viscosity.

2.1.2. Needle kinematics and dynamic mesh

In the present study, the needle is treated as a cantilever-like structure undergoing small bending deformation. The needle oscillation is prescribed rather than obtained by solving a structural dynamic equation, since the objective of the present work is to isolate and systematically examine the wake dynamics induced by needle oscillation. The prescribed motion is implemented through a self-developed UDF (User-Defined Function) and coupled to the dynamic mesh technique.

It should be emphasized that the prescribed motion consists of two separate components: the temporal motion of the needle tip and the spatial deformation profile of the needle. The needle-tip displacement is prescribed as a harmonic motion,

$$y_{\mathrm{tip}}(t) = A\sin(2\pi f t) \tag{4}$$

where A and f denote amplitude and frequency, respectively. Such a harmonic representation is motivated by experimental observations using X-ray phase-contrast imaging, which have revealed pronounced periodic radial oscillations of injector needles during injection [1].

For the parametric simulations, the deformation between the fixed end and the oscillating tip is modeled as a circular arc of constant needle length, to prescribe a smooth moving boundary rather than to represent the natural vibration mode. The sensitivity of the predicted wake dynamics to this prescribed bending profile was further assessed using the first bending mode of an ideal Euler–Bernoulli cantilever beam, as detailed in Appendix A.

The prescribed circular-arc deformation is expressed in polar coordinates as:

$$\begin{cases} r - 2r_0\cos\left(\theta - \dfrac{\pi}{2}\right) = 0, (0 \le \theta \le \alpha);\ 0 < t < \dfrac{T}{2} \\ r - 2r_0\cos\left(\theta - \dfrac{3\pi}{2}\right) = 0, (2\pi - \alpha \le \theta \le 2\pi);\ \dfrac{T}{2} < t < T \end{cases} \tag{5}$$

where r is the radial coordinate measured from the origin located at the fixed end of the needle, and θ denotes the angular coordinate. The needle tip reaches its maximum upward and downward amplitudes (A) at $t = T/4$ and $t = 3T/4$, respectively, and returns to the neutral equilibrium position at $t = T/2$ and $t = T$.

To accommodate the boundary deformation, the dynamic mesh technique with spring smoothing is used to update the mesh at each time step.

2.1.3. Computational setup

The computational domain is shown in Fig. 1(b), with a streamwise length of 100 mm (~28.5D) and a transverse width of 40 mm (~11.4D). The sensitivity of the numerical results to the transverse domain width is examined in Appendix B. The computational domain was discretized using an unstructured mesh. A mesh independence study was performed using three different base mesh sizes

(0.04 mm, 0.05 mm, and 0.0625 mm).

To verify grid independence under the vibration conditions considered in this study, two representative cases were examined: the maximum-amplitude case ($A = 0.9$ mm, $f = 10$ Hz) and the highest-frequency case ($A = 0.45$ mm, $f = 25$ Hz). The velocity and vorticity profiles along the cross-section at $x = 12D$ were compared at $t = 10T$, as shown in Fig. 3(a–d). For both cases, the velocity and vorticity profiles obtained using the three meshes exhibit good agreement, with only minor differences observed in the locally enlarged regions. In particular, the results obtained with the 0.05 mm mesh are in close agreement with those obtained with the finer 0.04 mm mesh, indicating that further mesh refinement has a limited influence on the results. Considering both computational cost and solution accuracy, a base size of 0.05 mm (approximately 1.6 million cells) was selected for the final simulations.

A uniform velocity inlet and pressure outlet were imposed as boundary conditions, while no-slip conditions were applied on all solid surfaces.

To solve the governing equations, a fully transient numerical framework was adopted. The pressure-velocity coupling was handled using the Pressure-Implicit with Splitting of Operators (PISO) algorithm. Spatial discretization adopted the Least Squares Cell Based method for gradient evaluation, a second-order scheme for pressure, and the Bounded Central Differencing scheme for momentum, while the temporal term was treated using a first-order implicit formulation. The time step (0.0002 s) was chosen such that the maximum Courant–Friedrichs–Lewy (CFL) number remained below 0.667, ensuring numerical stability throughout the transient simulation.

The present study primarily employs a 2D model assuming spanwise symmetry to isolate the key mechanisms governing the wake dynamics and enable systematic parametric analysis. The effects of three-dimensionality and the applicability of the 2D approximation are further assessed in Section 3.4.

2.2. Experiment setup

The experimental setup is illustrated in Fig. 4(a), where the needle is positioned inside an acrylic pipe. A specially designed needle was fabricated with a central through-hole and mounted on an additional supporting beam, with its cross-sectional view shown in Fig. 4(b). The additional supporting beam served only to impose a fixed boundary condition on the needle and was not treated as a

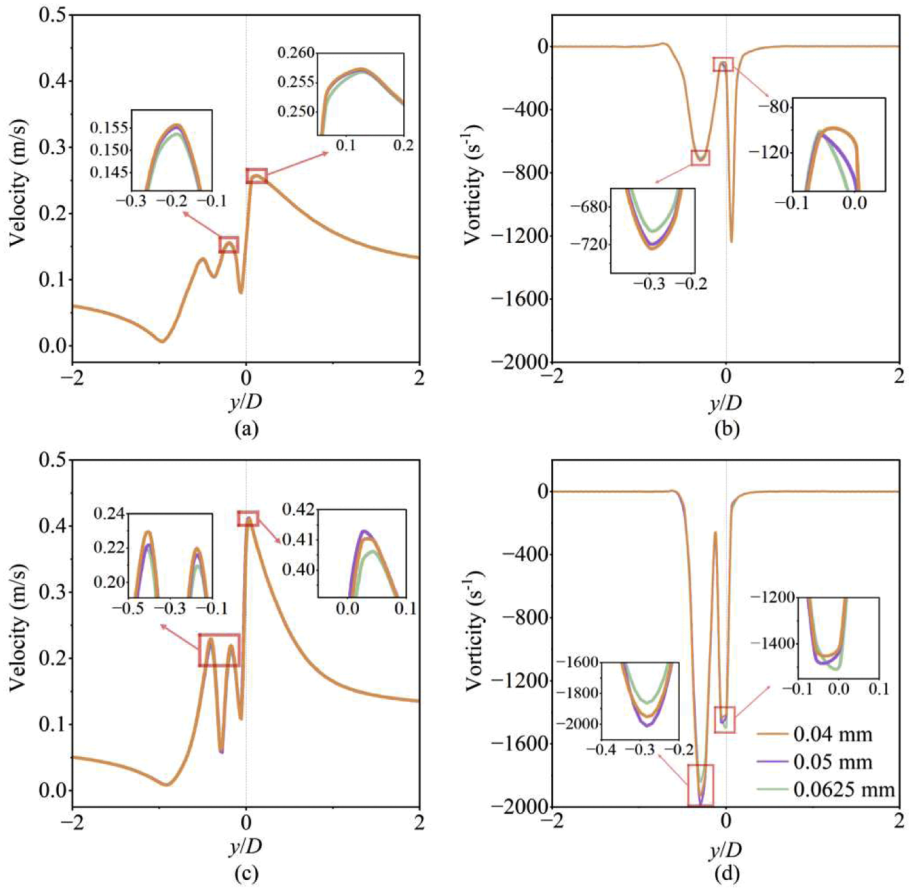


Fig. 3. Grid-independence comparison of velocity and vorticity profiles along $x = 12D$ at $t = 10T$ under two conditions: (a) $A = 0.9$ mm, $f = 10$ Hz, velocity; (b) $A = 0.9$ mm, $f = 10$ Hz, vorticity; (c) $A = 0.45$ mm, $f = 25$ Hz, velocity; and (d) $A = 0.45$ mm, $f = 25$ Hz, vorticity.

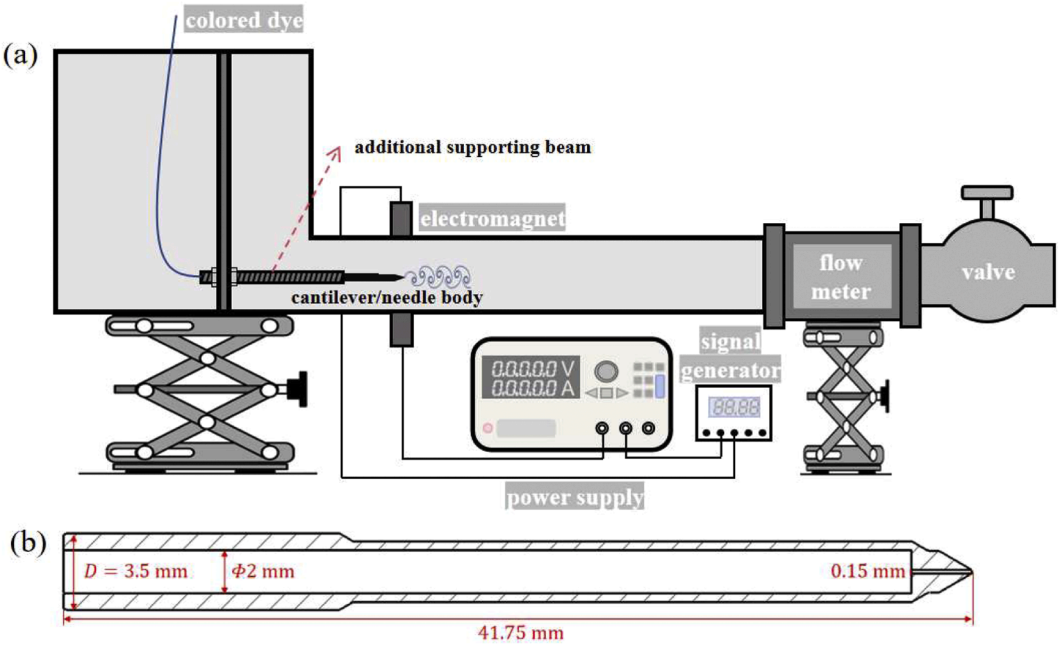


Fig. 4. Experimental apparatus and needle geometry: (a) Experimental setup and (b) hollow-needle configuration.

dynamic component in the numerical model. A transparent acrylic test section was used to provide optical access to the needle motion and the downstream dye traces.

Two direct-current (DC) electromagnets with equal magnetic attraction were positioned above and below the acrylic tube containing the needle. The electromagnets were alternately energized to generate periodic transverse oscillation of the needle at the prescribed frequency. This arrangement also reduced the influence of delayed release caused by residual magnetism.

A syringe pump was used to inject colored dye into the hollow needle. The dye was continuously released from the moving needle tip, and the release point followed the oscillatory motion of the needle, thereby providing a direct indication of its trajectory (rather than reproducing the fuel injection). After release, the dye was convected downstream and also provided qualitative information on the large-scale organization of the oscillation-induced wake.

The dye-exit velocity (~0.02 m/s) was slightly lower than both the inflow velocity and the maximum velocity of the vibrating needle tip, indicating that dye injection may locally affect the near-tip flow. Accordingly, the dye visualization is used only for qualitative assessment of the needle-tip motion and overall wake organization. Although the experiment was conducted in a 3D setup, the needle oscillation remained planar and perpendicular to the viewing direction, resulting in effectively 2D observations.

A direct imaging method was employed to record the needle motion and the downstream dye traces. A Phantom V7.3 complementary metal–oxide–semiconductor (CMOS) high-speed camera, equipped with a Nikon 105 mm lens, was used to capture the images at a frame rate of 20,000 fps and an exposure time of 50 μs. Water was used as the working fluid for safety and environmental considerations. Its density and dynamic viscosity at room temperature were approximately 1000 kg/m^3 and 1 mPa·s, respectively.

3. Results and discussion

3.1. Validation of the numerical model

To establish the reliability of the present simulations, the computational fluid dynamics (CFD) model is first quantitatively validated against published particle image velocimetry (PIV) measurements [31]. The present dye-visualization experiment is then used as a supplementary qualitative comparison of the large-scale wake behavior.

3.1.1. Comparison with literature PIV data

To quantitatively assess the capability of the numerical model in capturing the unsteady wake dynamics, the key non-dimensional geometric parameter of the vortex street, namely the vortex spacing ratio ($\bar{h}/\bar{l}$), was selected for validation. The simulated wake field was compared with the PIV measurements reported in Ref. [31] under similar Reynolds number and modified Strouhal number conditions.

A modified Strouhal number is introduced to account for both the oscillation frequency and amplitude

$$St_A = 2fA/U_0. \tag{6}$$

The spacing ratio was evaluated using a local interpolation method based on vortex core coordinates. For two consecutive same-signed vortices with coordinates $V_{t1}(X_{t1}, Y_{t1})$ and $V_{t2}(X_{t2}, Y_{t2})$, the local streamwise spacing is defined as

$$l_i = X_{t2} - X_{t1}. \tag{7}$$

The transverse spacing is obtained by interpolating the position of the upper vortex row at the streamwise location of the opposite-signed vortex $V_{b1}(X_{b1}, Y_{b1})$, yielding

$$h_i = \left| Y_{t_interp} - Y_{b1} \right| \tag{8}$$

where Y_{t_interp} denotes the interpolated vertical coordinate of the same-signed vortex row.

$$\bar{h} = \frac{1}{n} \sum_{i=1}^{n} h_i \tag{9}$$

$$\bar{l} = \frac{1}{n} \sum_{i=1}^{n} l_i \tag{10}$$

The spacing values were extracted over 3–4 consecutive shedding cycles, and the averaged ratio $\bar{h}/\bar{l}$ was used to represent the characteristic vortex spacing for each case.

The comparison between the present CFD results and the PIV measurements is shown in Fig. 5. All results exhibit highly similar wake patterns. The transverse-to-streamwise vortex spacing ratio ($\bar{h}/\bar{l}$) obtained from the simulations is close to the PIV measurements, as shown in Table 1.

Unlike the classical cross-flow wake of a circular cylinder, the terms "Kármán-type" and "reverse-Kármán-type" are used here only to describe wake topology based on the transverse positions of the two rows of oppositely rotating vortices. Reversal of the upper and lower positions of the two vortex rows indicates a reverse-Kármán-type wake, whereas vortices shed alternately at approximately the same transverse location define an aligned alternating-vortex wake.

In addition, the vorticity magnitude predicted by the CFD model is of the same order as the experimental values, although slightly higher. This difference can be attributed to the 2D numerical framework, which neglects 3D vortex stretching and the associated energy dissipation, allowing vortices to maintain a somewhat stronger intensity.

The good agreement in vortex street morphology, spacing ratio, and vorticity magnitude demonstrates that the present numerical model can reliably capture the essential wake dynamics and vortex evolution of the oscillating needle.

To assess the applicability of the present 2D framework near the upper end of the investigated Reynolds-number range, a benchmark simulation of 2D flow past a stationary circular cylinder at $Re = 1000$ was performed. Good agreement with the 2D direct numerical simulation (DNS) results reported in of Ref. [40] supports the reliability of the framework, with details provided in Appendix C.

3.1.2. *Supplementary qualitative visualization of the oscillation-induced wake*

To further illustrate the wake behavior associated with the oscillating needle, the present dye-visualization results are compared qualitatively with the numerical predictions.

As depicted in Fig. 6, under the same Re and St_A conditions, both the dye-visualization results and the simulated vorticity contours clearly capture an alternating vortex shedding pattern (like reverse-Kármán-type wake) in the near-wake region. Furthermore, at $Re = 105$ and $St_A = 0.33$, both the experiment and the numerical simulation show a pronounced upward deflection of the overall wake from the centerline.

It should be noted that the dye patterns represent the trajectories of dye continuously released from the moving needle tip rather than the instantaneous vortex cores in the flow field. Therefore, the experimental images are used only to compare large-scale wake features, such as the alternating wake organization and overall wake-deflection direction, rather than local quantities such as core position, size, strength, or downstream spacing.

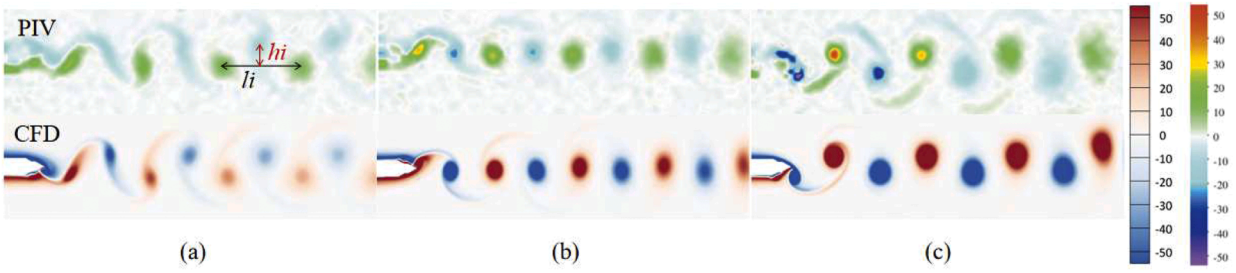


Fig. 5. Comparison of vorticity contours between the present CFD results and experimental PIV data [31]. (a) $Re = 255$, $St_A = 0.0792$; (b) $Re = 255$, $St_A = 0.1562$; (c) $Re = 255$, $St_A = 0.2354$.

Table 1
Comparison of the present CFD results and experimentally measured data [31].

Conditions	Method	$\bar{h}/\bar{l}$	Error	Mode
(i) $Re = 255$, $St_A = 0.0792$	Ref. [31]	0.257	4.79%	Kármán-type wake
	Present study	0.26932		
(ii) $Re = 255$, $St_A = 0.1562$	Ref. [31]	0.05	4%	Aligned alternating-vortex wake
	Present study	0.052		
(iii) $Re = 255$, $St_A = 0.2354$	Ref. [31]	0.207	6.76%	Reverse-Kármán-type wake
	Present study	0.193		

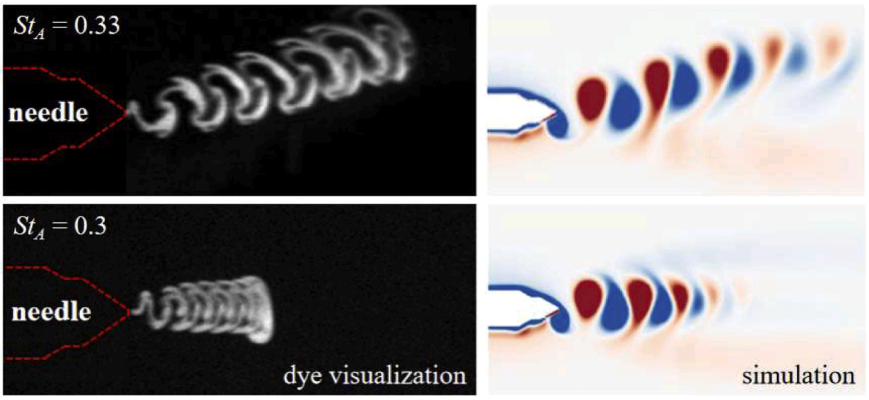


Fig. 6. Qualitative comparison between dye visualization and CFD results.

The present dye visualization thus provides supplementary qualitative support for the wake behavior predicted numerically, whereas quantitative validation of the numerical model is established independently through comparison with the PIV measurements in Section 3.1.1.

3.2. Wake dynamics induced by the oscillating needle

Building on the validated numerical framework, a systematic parametric study is conducted to investigate the effects of needle kinematics and fluid properties on the wake evolution, transition regimes, and the corresponding transient forces acting on the needle.

3.2.1. Effect of amplitude on wake characteristics

To isolate the effect of oscillation amplitude on the wake dynamics, simulations were performed at $Re = 350$, $f = 10$ Hz, and $U_0 = 0.1$ m/s, with A varied from 0.3 mm to 0.9 mm. Fig. 7 shows the corresponding instantaneous ($t = 1$ s) vorticity, velocity, and pressure-fluctuation fields.

As shown in Fig. 7, the wake flow characteristics undergo a fundamental transition with increasing oscillation amplitude. The velocity magnitude in the wake generally increases with amplitude, while low-velocity regions are observed near the vortex cores. At lower amplitudes (the middle column of Fig. 7(a) and (b)), these low-speed regions gradually merge into a continuous velocity-deficit band due to the small inter-vortex spacing. Macroscopically, this streamwise momentum deficit indicates a drag force on the needle. However, at larger amplitudes, the wake transitions from a drag-producing to a thrust-producing regime. Meanwhile, the inter-vortex spacing increases and distinct high-velocity bands emerge, as shown in the middle column of Fig. 7(d) and (e).

The pressure fluctuation is defined as the deviation of the instantaneous pressure from its time-averaged value.

$$p' = p - \bar{p} \tag{11}$$

where p denotes the instantaneous pressure and $\bar{p}$ represents the time-averaged pressure.

The pressure fluctuation contours reveal the unsteady response of the wake to the imposed needle oscillation at different amplitudes. Although periodic vortex shedding occurs at all amplitudes, weak pressure fluctuations at small amplitudes remain confined to the near-wake region and decay rapidly downstream. At larger amplitudes, stronger oscillation-induced disturbances result in more intense pressure fluctuations that persist over a much larger portion of the wake. This behavior reflects enhanced momentum transfer from the oscillating needle to the surrounding fluid.

Following the global wake analysis, the local flow near the needle tip, where the oscillating needle directly drives the surrounding fluid, is examined to clarify its amplitude-dependent response. Flow variables are extracted within a $3D \times 3D$ region surrounding the tip and along a line at $x = 12D$ (Fig. 1).

Fig. 8 shows the normalized velocity magnitude (U/U_0) along the line at $x = 12D$ for different oscillation amplitudes, where $U = ||$

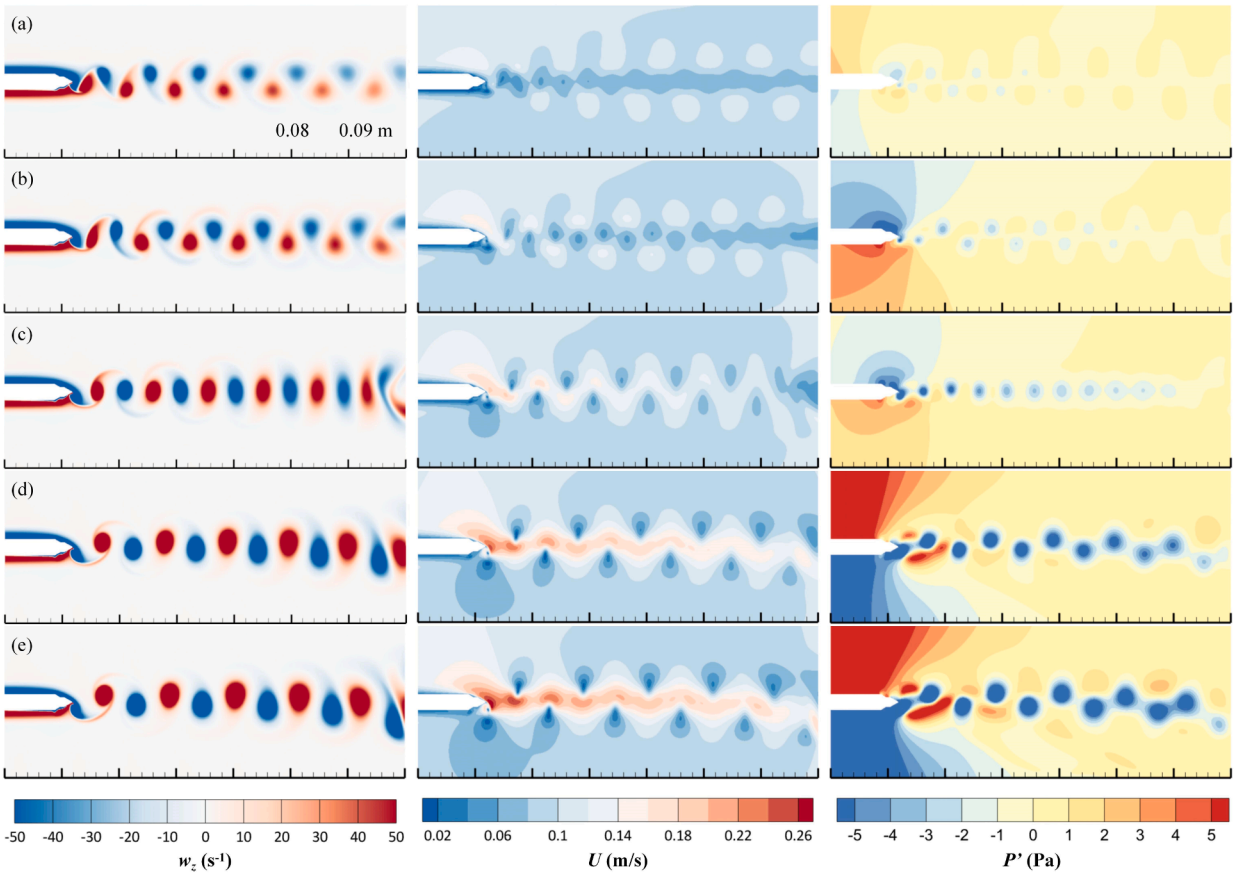


Fig. 7. Contours of vorticity, velocity, and pressure fluctuation at different oscillation amplitudes: (a) 0.3 mm, $St_A = 0.06$; (b) 0.45 mm, $St_A = 0.09$; (c) 0.6 mm, $St_A = 0.12$; (d) 0.8 mm, $St_A = 0.16$; and (e) 0.9 mm, $St_A = 0.18$. From left to right, the columns show vorticity (s^{-1}), velocity (m/s), and pressure fluctuation (Pa), respectively.

$\mathbf{u}|| = \sqrt{u_x^2 + u_y^2}$ denotes the local velocity magnitude. Pronounced non-monotonic variations develop near the needle tip and become progressively stronger with increasing oscillation amplitude.

This behavior can be interpreted from the instantaneous velocity contours in Fig. 9. For the representative amplitudes shown, a pronounced asymmetric velocity distribution develops near the needle tip. During the upward motion of the needle, the effective upper flow passage contracts, accelerating the local flow. The rapid acceleration and turning of the flow promote local separation near the tip, leaving a low-velocity recirculation region above it. Conversely, the flow passage on the lower side expands, and the upward-moving needle entrains the adjacent fluid while redistributing the local flow, producing a high-velocity region below the tip. A corresponding asymmetric pattern, with the upper and lower flow features reversed, occurs at $3T/4$.

During the $T/4$ to $T/2$ interval, the needle moves downward from its maximum upward displacement toward the equilibrium position. This motion constricts the lower flow passage and accelerates the fluid below the tip. The accelerated flow is deflected and the associated shear layer rolls up into a counterclockwise-rotating vortex. With increasing oscillation amplitudes, this effect intensifies and local acceleration and vortex-induced disturbance become stronger. At $T/2$, the velocity profiles in Fig. 8 exhibit multiple local peaks and troughs near the needle tip. These extrema correspond to the alternating high- and low-velocity regions produced by local flow acceleration, vortex-induced motion, and flow separation. The velocity evolution observed at phase T is likewise attributable to the mechanism above, with the upper and lower flow structures reversed as the direction of needle motion changes.

At a fixed oscillation period, increasing the amplitude increases the characteristic needle velocity and strengthens the momentum transfer to the surrounding fluid. Consequently, larger amplitudes generally produce stronger velocity variations and steeper local velocity gradients.

Fig. 10 compares the temporal evolution of the spatially averaged near-tip velocity and the domain-averaged enstrophy for different oscillation amplitudes. The near-tip averaging region is highlighted by the blue box in Fig. 1. The spatially averaged near-tip velocity is defined as

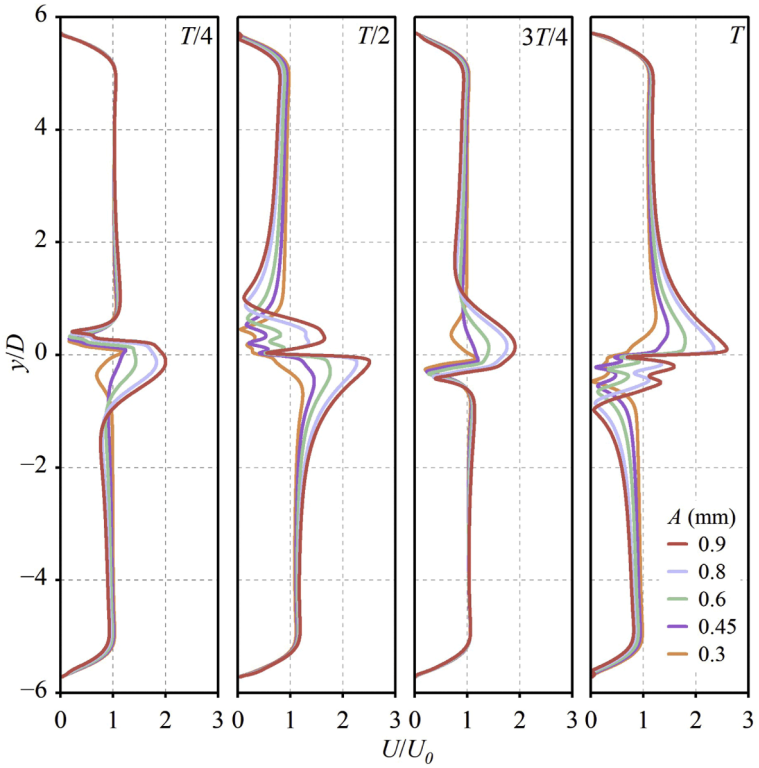


Fig. 8. The velocity distribution at $x = 12D$ under different amplitudes.

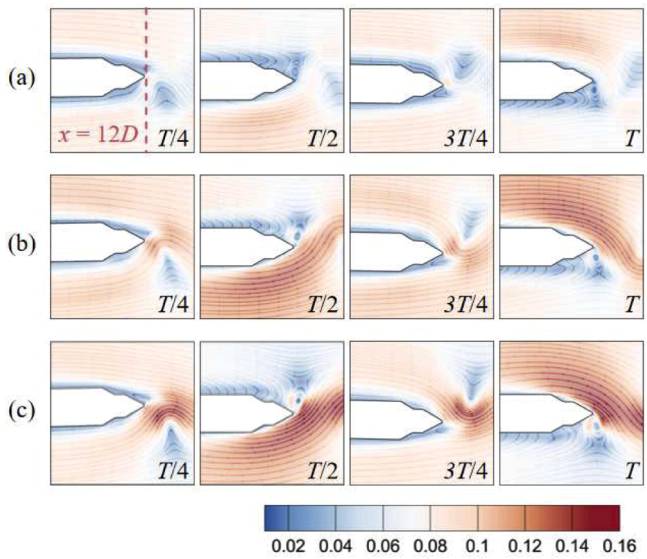


Fig. 9. The velocity distribution contours at four time instants for different oscillation amplitudes: (a) $A = 0.3$ mm, (b) $A = 0.45$ mm, and (c) $A = 0.6$ mm.

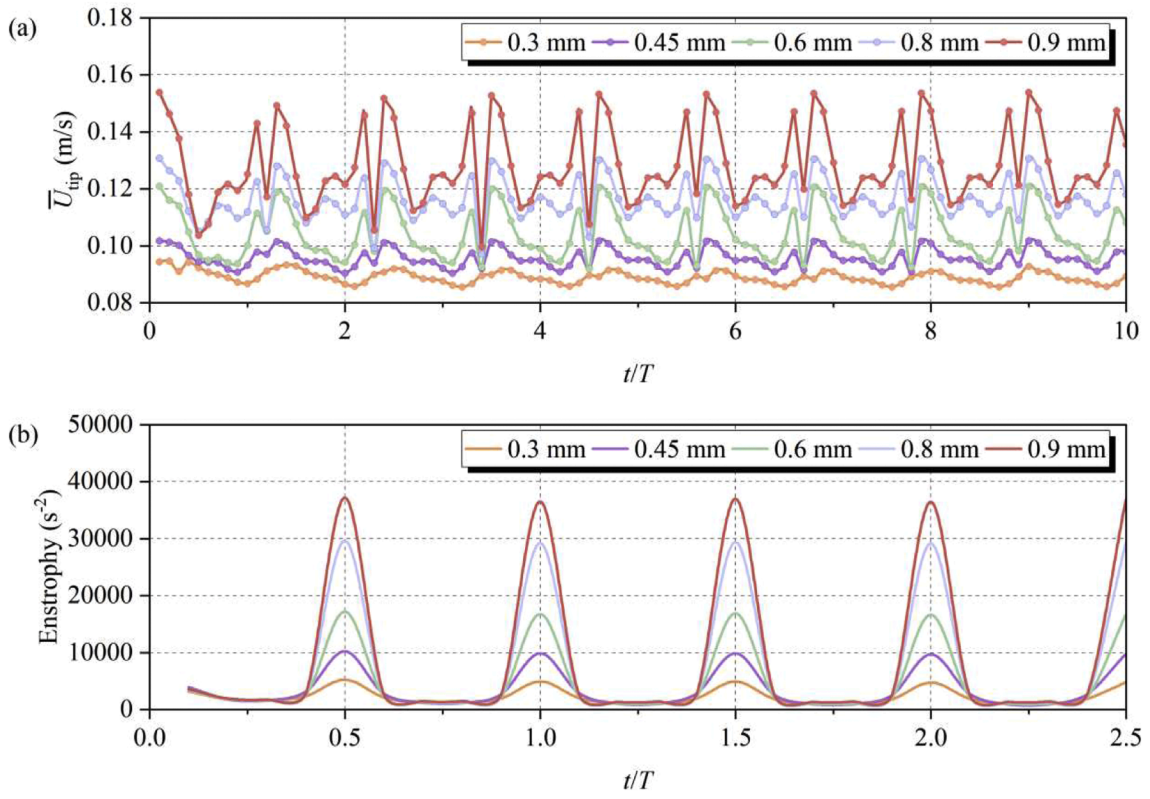


Fig. 10. Temporal evolution of (a) the near-tip spatially averaged velocity and (b) the domain-averaged enstrophy at different amplitudes. The time axis is normalized by the vibration period T.

$$\overline{U}_{\text{tip}}(t) = \frac{1}{S_{\text{tip}}} \int_{S_{\text{tip}}} U \mathrm{d}A \tag{12}$$

where S_{tip} is the area of the near-tip sampling region. As shown in Fig. 10(a), the near-tip velocity exhibits a periodic response, with both its mean value and fluctuation amplitude increasing with oscillation amplitude.

In the present study, the domain-averaged enstrophy is defined over the entire computational domain as:

$$\text{Enstrophy} = \frac{1}{S_{\text{domain}}} \int ||\mathbf{w}||^2 \mathrm{d}A \tag{13}$$

$$\frac{\mathrm{d}\mathbf{w}}{\mathrm{d}t} = (\mathbf{w} \cdot \nabla)\mathbf{u} + \nu \nabla^2 \mathbf{w} \tag{14}$$

where S_{domain} denotes the area of the entire computational domain, and $\mathbf{w}$ is the vorticity.

For the 10 Hz condition, one oscillation cycle corresponds to $T = 0.1$ s. The enstrophy peaks recur approximately every half-cycle, coinciding with the phases of maximum needle speed. At these phases, the strong needle motion generates large velocity gradients and enhanced vorticity near the needle, leading to the shedding of stronger vortical structures and hence higher domain-averaged enstrophy. At a fixed oscillation frequency, as the amplitude increases, the resulting flow disturbances intensify, accelerating the surrounding fluid and thereby enhancing the local velocity gradient. Consequently, increasing the oscillation amplitude enhances near-wall vorticity generation and shear-layer roll-up, producing stronger vortical structures and a higher domain-averaged enstrophy. In the present two-dimensional model, the vortex-stretching term vanishes.

3.2.2. *Effects of frequency on wake characteristics*

In addition to amplitude, oscillation frequency is another key parameter governing the wake dynamics. In this study, the oscillation frequency of the needle is defined as the number of complete oscillation cycles per unit time. Frequency effects were examined at $A = 0.45$ mm and $U_0 = 0.1$ m/s ($Re = 350$). Fig. 11 shows the instantaneous contours of vorticity, velocity, and pressure fluctuations at $t = 1$ s for $f = 10$–25 Hz, with the corresponding St_A values indicated in the figure.

With increasing oscillation frequency, the wake structure undergoes a transition from a Kármán-type wake (left column of Fig. 11 (a) and (b)) to an asymmetric reverse-Kármán-type wake (left column of Fig. 11(d)–(F)), through an intermediate state characterized

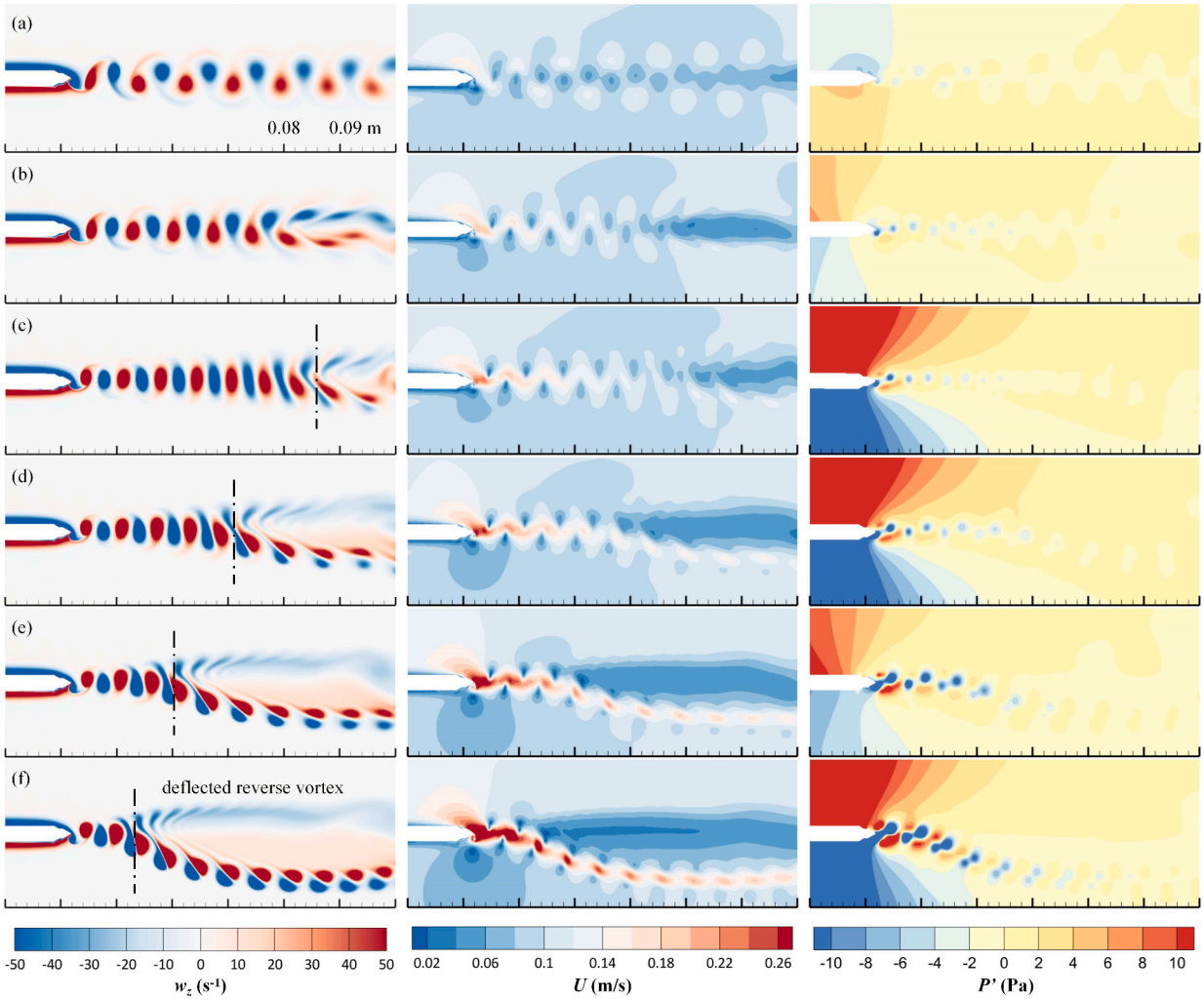


Fig. 11. Contours of vorticity, velocity, and pressure fluctuation at different oscillation frequencies: (a) 10 Hz, $St_A = 0.09$; (b) 13 Hz, $St_A = 0.117$; (c) 15 Hz, $St_A = 0.135$; (d) 17 Hz, $St_A = 0.153$; (e) 20 Hz, $St_A = 0.18$; and (f) 25 Hz, $St_A = 0.225$. From left to right, the columns show vorticity (s^{-1}), velocity (m/s), and pressure fluctuation (Pa), respectively.

by an aligned vortex pattern (left column of Fig. 11(c)). This transition reflects the increasing relative importance of oscillation-induced transverse forcing compared with streamwise wake convection. At low St_A, the transverse needle motion is relatively weak, and the vortices remain predominantly arranged on their original sides of the wake. As St_A increases, the stronger transverse motion progressively modifies the vortex formation and shedding positions, leading first to an aligned wake and eventually to a reverse-Kármán-type wake.

At low frequencies, the large inter-vortex spacing allows the shed vortices to convect downstream with relatively weak mutual interaction. As the frequency increases, the vortex spacing decreases, leading to intense vortex interactions before sufficient convection occurs. When the mutual induced velocity becomes dominant, the stability of the symmetric vortex arrangement is weakened, triggering a wake deflection (left column of Fig. 11(c)–(F)). This symmetry-breaking phenomenon is consistent with Dynnikova [34], who attributed wake symmetry disruption to flow instability under bending perturbations. In this regime, small asymmetric perturbations may grow and develop into a persistently deflected wake. Furthermore, the onset point of the wake deflection moves upstream towards the needle with increasing frequency, as indicated by the black dash-dotted lines in the left column of Fig. 11(c)–(F).

Increasing the oscillation frequency of the needle increases its kinematic velocity, which in turn accelerates the surrounding fluid and raises the mean wake velocity. Meanwhile, pressure fluctuations, initially confined to the near-wake, extend further downstream due to the more intense disturbances (right column of Fig. 11(a)–(F)).

To facilitate comparison among different excitation conditions, the time variable is nondimensionalized by the excitation period, i.e., t/T, where $T = 1/f$. To quantify the near-field dynamics, Fig. 12(a) presents the temporal evolution of the spatially averaged velocity magnitude in the needle-tip region. The oscillation frequency determines the periodicity of the local velocity response. The cyclic appearance of velocity peaks and troughs results from the continuous downstream convection of the wake structures. As high-speed

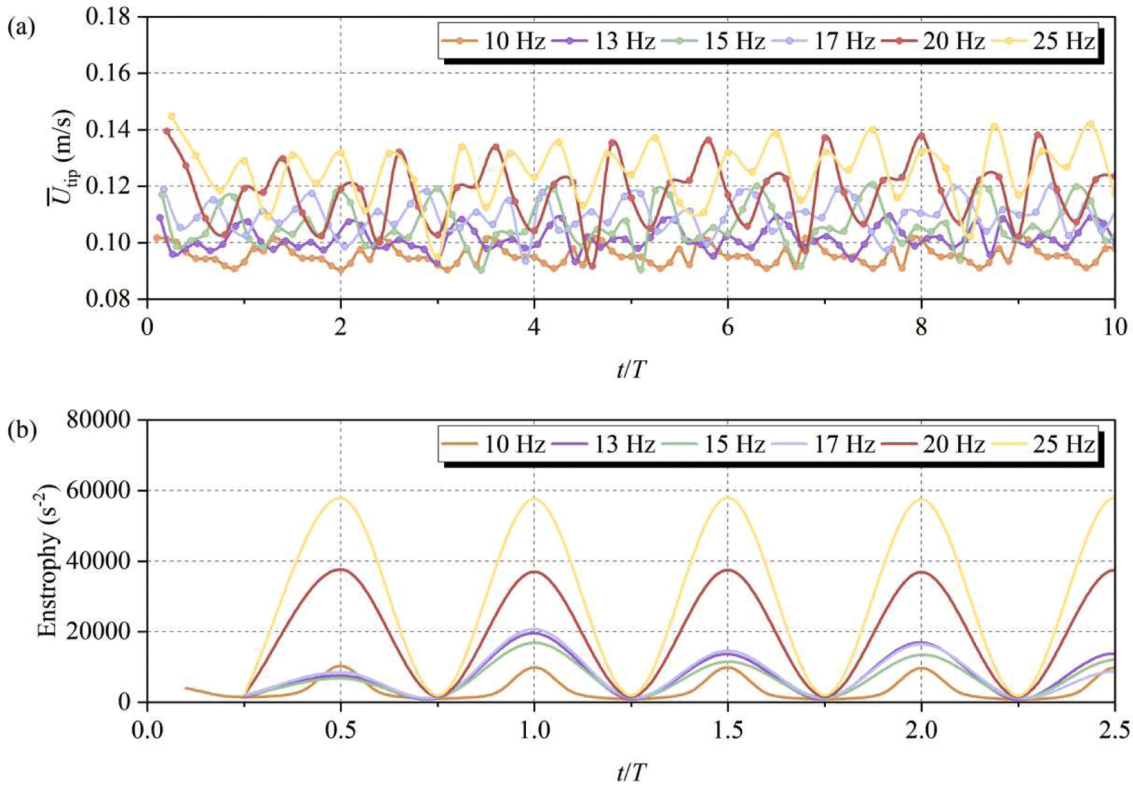


Fig. 12. Temporal evolution of (a) the near-tip spatially averaged velocity and (b) the domain-averaged enstrophy at different frequencies. For each frequency, the time axis is normalized by the corresponding vibration period $T = 1/f$.

and low-speed fluid regions are periodically generated, they sequentially pass through and exit this localized zone, driving the cyclic velocity fluctuations. Furthermore, a higher frequency not only elevates the absolute values of the velocity peaks but also markedly amplifies the peak-to-trough fluctuation range. This demonstrates that high-frequency oscillations impart both greater mean kinetic energy and intensified cyclic pulsations to the downstream fluid.

Fig. 12(b) depicts the temporal evolution of global enstrophy. The cyclic variation of enstrophy is strongly influenced by the oscillation frequency. Within each oscillation cycle, the enstrophy reaches its peaks at the $T/2$ and T phases, corresponding to the instants of maximum needle mechanical velocity and strongest fluid shear, while the troughs occur at the $T/4$ and $3T/4$ phases when the needle velocity drops to zero. Increasing oscillation frequencies increases the characteristic needle velocity ($\sim 2\pi fA$), strengthening the local velocity gradient and vorticity generation and thereby increasing global enstrophy.

3.2.3. *Effect of inflow velocity on wake characteristics*

The effects of inflow velocity were examined over $U_0 = 0.03$–0.10 m/s at fixed $A = 0.45$ mm and $f = 10$ Hz. The corresponding Re and St_A values are indicated in the figure. Fig. 13 shows the instantaneous contours of vorticity, velocity, and pressure fluctuations at $t = 1$ s.

At a low inflow velocity ($U_0 = 0.03$ m/s, left column of Fig. 13(a)), the weak freestream convection causes the shed vortices to remain near the needle tip, resulting in a compact concentration of vortical structures. Consequently, vortices generated during subsequent oscillation cycles interact strongly with the previously shed structures, modifying their downstream evolution and trajectories.

As the inflow velocity increases to 0.07 m/s and beyond (left column of Fig. 13(d)–(F)), the vortex street exhibits two successive spatial reorganizations. Taking $U_0 = 0.07$ m/s (left column of Fig. 13(d)) as an example, the wake is sequentially divided into three regions. The main near-wake vortex street first transitions into a two-layered vortex street (black solid lines). Further downstream, a second transition occurs (black dotted lines) where the two-layered structure reorganizes into a secondary vortex street, featuring enlarged vortices and a reduced shedding frequency. With increasing inflow velocity, stronger streamwise convection transports the vortices downstream more rapidly, increasing the inter-vortex spacing. Consequently, both transition boundaries migrate downstream, and counting the shed vortex dipoles confirms a delay in the temporal onset of the initial transition.

As the flow velocity increases from 0.05 m/s to 0.09 m/s, the wake transitions from a reverse-Kármán-type wake to a Kármán-type wake. This transition arises from the competition between incoming flow inertia and the oscillation-induced disturbances. As velocity increases, the higher Re amplifies the inertial effects of the fluid. The enhanced freestream momentum suppresses the formation of the

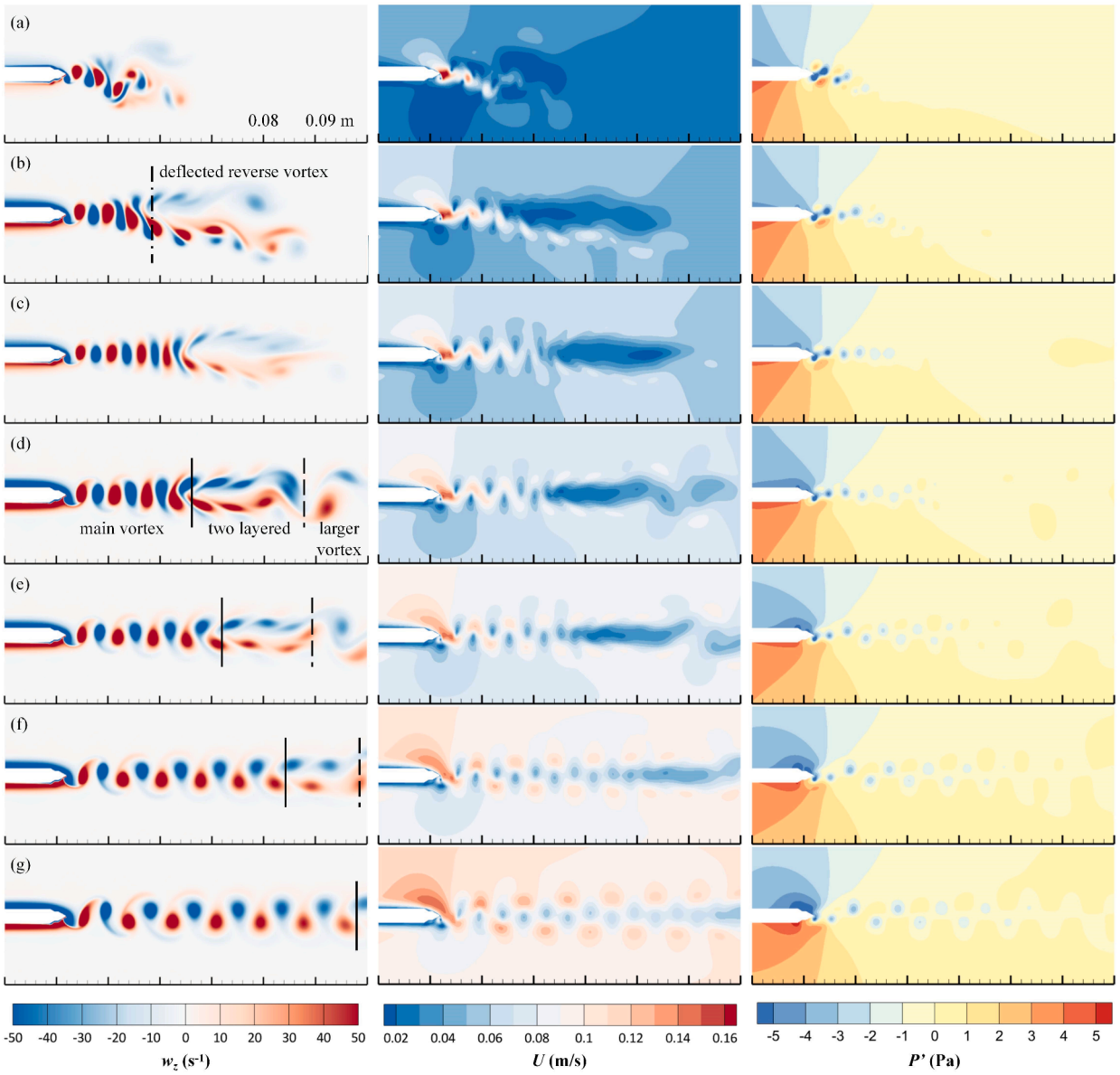


Fig. 13. Contours of vorticity, velocity, and pressure fluctuation at different inflow velocities: (a) 0.03 m/s, $St_A = 0.3$, $Re = 105$; (b) 0.05 m/s, $St_A = 0.18$, $Re = 175$; (c) 0.06 m/s, $St_A = 0.15$, $Re = 210$; (d) 0.07 m/s, $St_A = 0.129$, $Re = 245$; (e) 0.08 m/s, $St_A = 0.1125$, $Re = 280$; (f) 0.09 m/s, $St_A = 0.1$, $Re = 315$; and (g) 0.1 m/s, $St_A = 0.09$, $Re = 350$. From left to right, the columns show vorticity (s^{-1}), velocity (m/s), and pressure fluctuation (Pa), respectively.

oscillation-driven reverse vortex street.

As shown in Fig. 14, the normalized velocity profiles exhibit weaker near-tip variations as inflow velocity increases. At low velocities, weak streamwise convection allows vortices generated by needle oscillation to remain near the tip for a longer time, promoting stronger vortex interactions and local flow disturbances. Conversely, higher inflow velocities strengthen downstream convection and reduce vortex accumulation near the tip, leading to a weaker normalized velocity response. This trend is also consistent with the decrease in St_A as U increases, indicating a reduced relative influence of the oscillation-induced transverse motion.

Fig. 15(a) shows that, at low inflow velocities (0.03–0.06 m/s), the averaged velocity near the tip exceeds the inflow velocity, indicating a strong contribution from the oscillation-induced local flow. As inflow velocity increases (0.09–0.1 m/s), the local average velocity is suppressed and falls below the inflow velocity. Because A and f are fixed, the needle velocity remains unchanged, whereas stronger streamwise convection reduces the influence of the oscillation.

Fig. 15(b) shows that the global enstrophy varies only weakly with inflow velocity, exhibiting a slight overall increase. Over the present range of inflow velocities, the overall vortical activity is less strongly affected by inflow velocity than by the oscillation

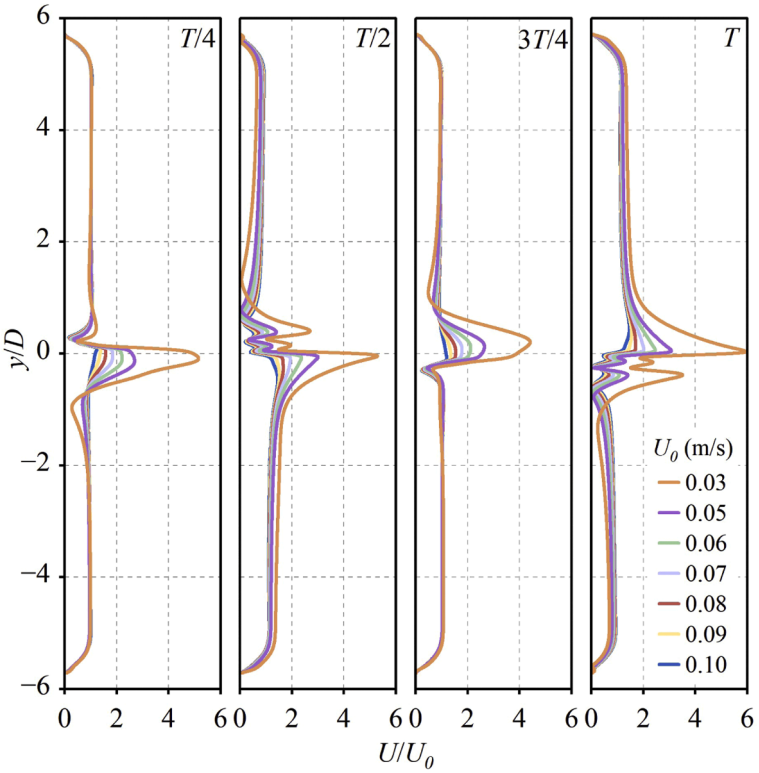


Fig. 14. The velocity distribution at $x = 12D$ under different velocities.

parameters. With the amplitude and frequency fixed, an increased inflow velocity primarily accelerates the downstream convection of the shed vortices, rather than strengthening their rotational intensity.

3.2.4. *Effect of density and viscosity on wake characteristics*

As shown in Fig. 16, the effects of fluid density and viscosity on the wake were examined at fixed $A = 0.45$ mm, $U_0 = 0.07$ m/s, and $f = 10$ Hz. The corresponding fluid properties are listed in Table 2, while *Re* is indicated in the figure and St_A remains constant at 0.129.

Fig. 16 illustrates that, under identical excitation conditions, the wake structures generated by different fluids vary significantly. Due to its substantially higher viscosity, diesel corresponds to a lower *Re* and stronger viscous diffusion. This can accelerate the attenuation of oscillation-induced disturbances and suppress the roll-up and interaction of the separated vorticity layers. As a result, the wake manifests merely as two approximately parallel rows of vortices. As viscosity decreases and the *Re* increases, the reduced viscous damping allows stronger vortex roll-up and interaction, leading to wake modes including Kármán-type, aligned alternating-vortex, and reverse-Kármán-type wake. These results demonstrate a strong dependence of the wake topology on Re under otherwise identical excitation conditions. Accordingly, Section 3.2.5 introduces needle oscillation parameters, inflow velocity, density, and kinematic viscosity to characterize the wake across different St_A and *Re*.

Further analysis of the velocity contours in Fig. 16 reveals a strong dependence of wake velocity propagation on fluid viscosity. Fluids with lower viscosity exhibit weaker viscous dissipation, enabling the oscillation-induced disturbances to persist further downstream. Conversely, in highly viscous fluids such as diesel and n-dodecane, strong dissipative forces rapidly attenuate the wake velocity, confining the high-speed regions primarily to the near wake. Similarly, the contours of pressure fluctuation demonstrate an identical spatial trend.

Fig. 17 presents the dimensionless velocity profiles at $x = 12D$ for different working fluids. As viscosity increases, the boundary layer effect becomes more pronounced, leading to a greater viscous shear and less steep velocity gradients. This trend is particularly evident near the upper and lower walls, where the slopes of velocity profiles become progressively gentler. Among all the evaluated fluids, the velocity profile in diesel deviates most noticeably from the others, despite exhibiting a similar overall trend. This difference is associated with the stronger viscous diffusion and lower Re of diesel, which suppress vortex development and attenuate the oscillation-induced velocity disturbances. Consequently, the normalized velocity near the tip is significantly lower for diesel than for the other fluids.

The temporal evolution of the average velocity near the tip for different working fluids is illustrated in Fig. 18(a). In the diesel case, the average velocity exhibits an overall decreasing trend. For n-dodecane, the decreasing trend is slight. By contrast, other lower-viscosity fluids generally maintain a relatively stable or even slightly increasing velocity response over time. These differences are primarily attributed to variations in fluid viscosity. Diesel and n-dodecane, with higher viscosities, experience stronger viscous

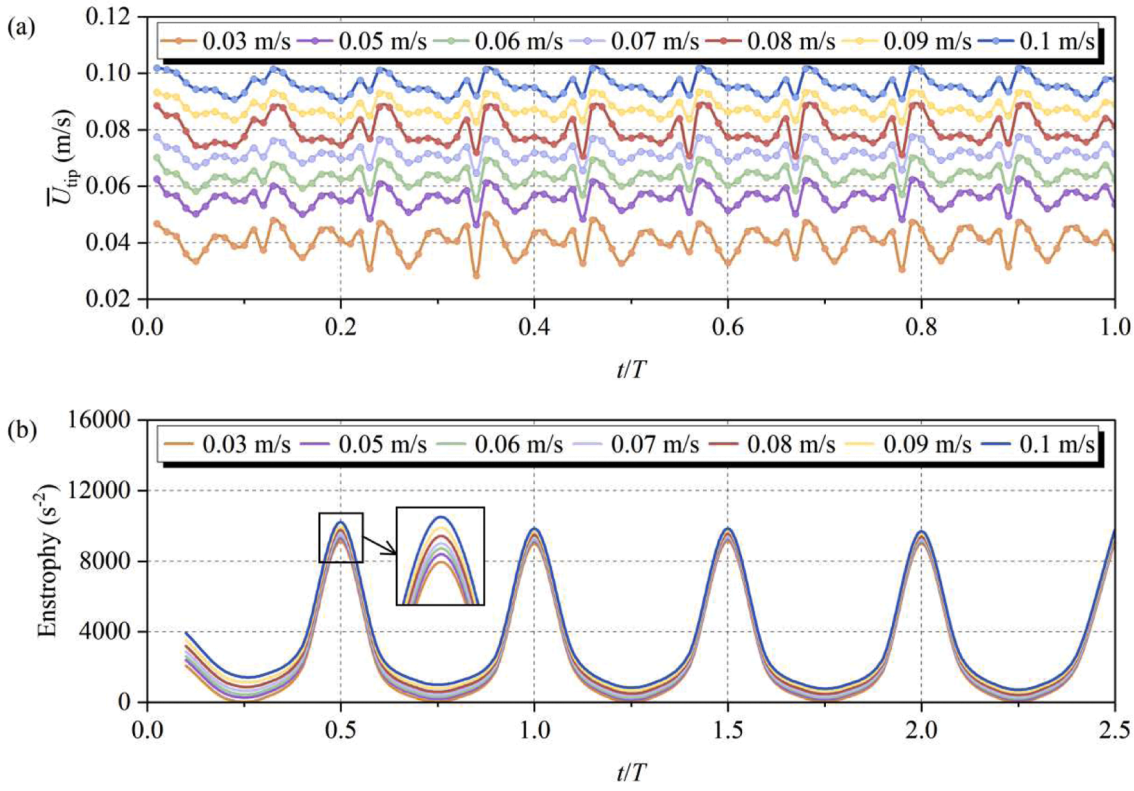


Fig. 15. Temporal evolution of (a) the near-tip spatially averaged velocity and (b) the domain-averaged enstrophy at different velocities.

diffusion, resulting in a sustained decline in velocity.

Fig. 18(b) evaluates the global enstrophy for the different working fluids. The enstrophy exhibits relatively weak sensitivity to fluid properties, with a slight overall decrease as the viscous influence increases. Reduced viscous diffusion in the lower-viscosity cases allows the generated vortical structures to persist longer, whereas stronger diffusion promotes faster attenuation of vorticity, resulting in slightly lower domain-averaged enstrophy.

3.2.5. Wake-Pattern transition and regime map

The preceding results indicate that variations in amplitude, frequency, inflow velocity, and fluid properties significantly alter the wake patterns induced by needle oscillation. To systematically characterize these transitions, additional numerical simulations were performed over a range of *Re* and St_A, as summarized in Fig. 19. The diamonds denote the Kármán-type wake, squares indicate the aligned alternating-vortex wake, and triangles represent the reverse-Kármán-type wake, with Points A, B, and C illustrating representative patterns of the three regimes.

Using the aligned alternating-vortex wake to approximate the transition boundary, an empirical power-law relation was obtained by fitting the numerical data (dashed line):

$$Re = 3.25 St_A^{-2.24} \tag{15}$$

where, $Re = \rho U_0 D/\mu$, $St_A = 2Af/U_0$, $D = 3.5$ mm, $\nu = \mu/\rho$. By rearranging and simplifying the terms, Eq. (15) can be rewritten as:

$$\frac{(Af)^{2.24}}{U_0^{1.24}} = 196.566\nu \tag{16}$$

To further validate the transition trend, several experimental and numerical results reported in previous studies [31,32] were converted to the modified St_A and superimposed on the present *Re*-St_A transition map for comparison, showing good qualitative agreement with the predicted boundary.

As observed from Fig. 19, under fixed oscillation parameters, a decrease in the *Re* favors the formation of the Kármán-type wake. Conversely, an increase in inflow velocity simultaneously increases *Re* and decreases St_A, thereby also driving the wake towards a Kármán-type wake pattern. Moreover, the fitted boundary shows that the transition *Re* decreases with increasing St_A, indicating that stronger oscillatory forcing promotes the reverse-Kármán-type wake at progressively lower *Re*.

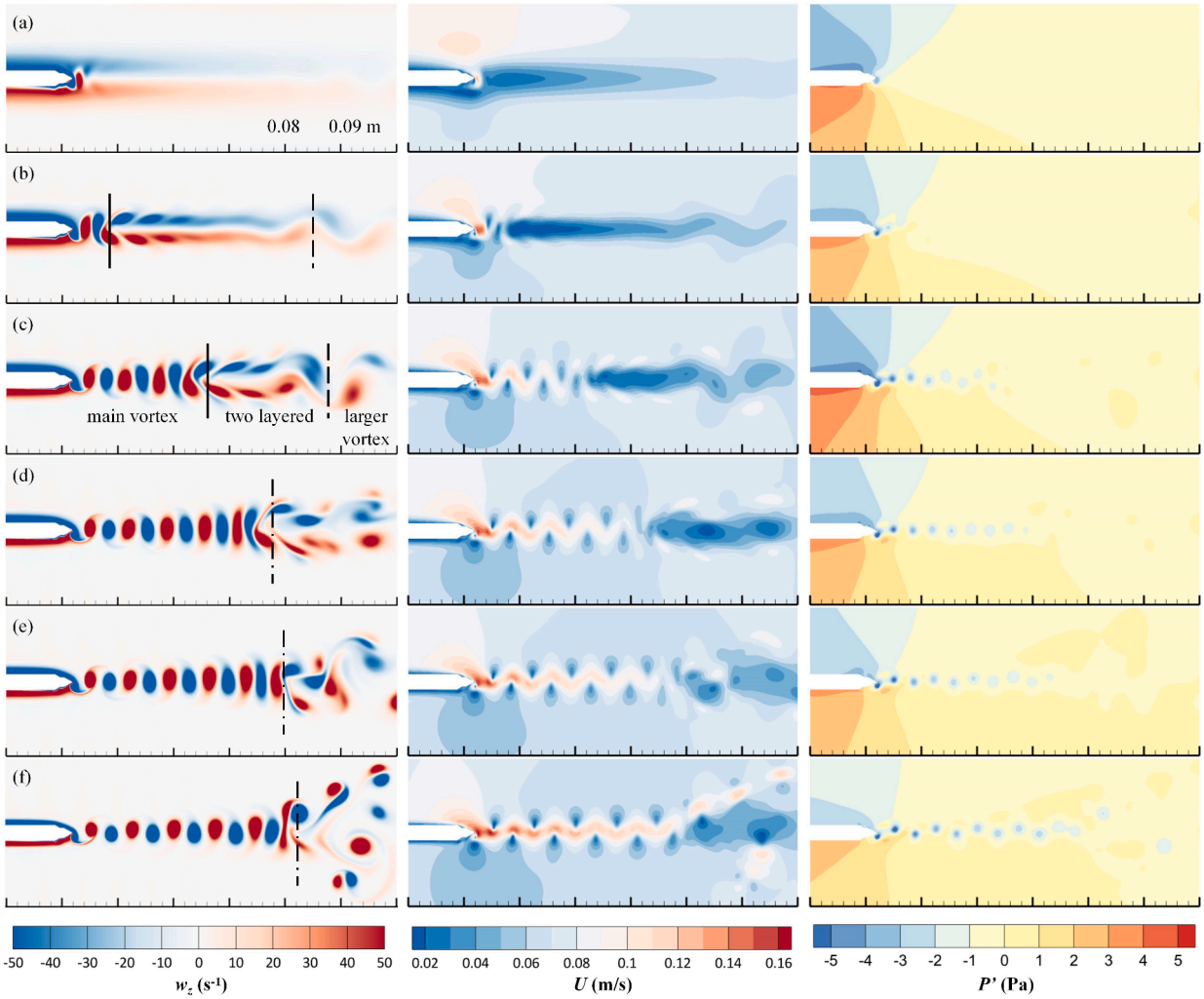


Fig. 16. Contours of vorticity, velocity, and pressure fluctuation with different fluids: (a) diesel, $Re = 55$; (b) n-dodecane, $Re = 134.4$; (c) water, $Re = 243.8$; (d) methanol, $Re = 350$; (e) gasoline, $Re = 445.8$; and (f) liquid ammonia, $Re = 983.2$. From left to right, the columns show vorticity (s^{-1}), velocity (m/s), and pressure fluctuation (Pa), respectively.

Table 2
Density and viscosity parameters of different fluids.

Fluid	diesel	gasoline	n-dodecane	water	liquid ammonia	methanol
Density (kg/m^3)	848	746	745.8	998.2	610	785
Dynamic viscosity (mPa·s)	3.78	0.41	1.36	1.003	0.152	0.5495

3.3. Wake generation, tip-geometry effects, and hydrodynamic forces

3.3.1. Geometric sensitivity of wake structures

To assess the sensitivity of the oscillation-induced wake to the needle-tip geometry, six representative tip configurations (Shapes 0–5; Fig. 20) were examined under identical operating conditions. Water was used as the working fluid, with $f = 10$ Hz, $A = 0.45$ mm, and $U_0 = 0.1$ m/s, corresponding to $Re = 350$ and $St_A = 0.09$. Shape 0 is the baseline geometry used in the preceding sections, whereas Shapes 1–5 represent variations in tip angle, truncation, and curvature.

Fig. 20 compares the instantaneous vorticity, velocity, and pressure-fluctuation fields for the six tip geometries at $t = 1$ s. Despite the marked variations in the local tip geometry, all configurations exhibit a similar overall wake topology. Alternating vortices are generated near the tip and convected downstream, forming a spatially periodic vortex street. Farther downstream, the initially distinct primary vortices gradually weaken and evolve into a two-layered wake structure. Thus, under the present operating condition,

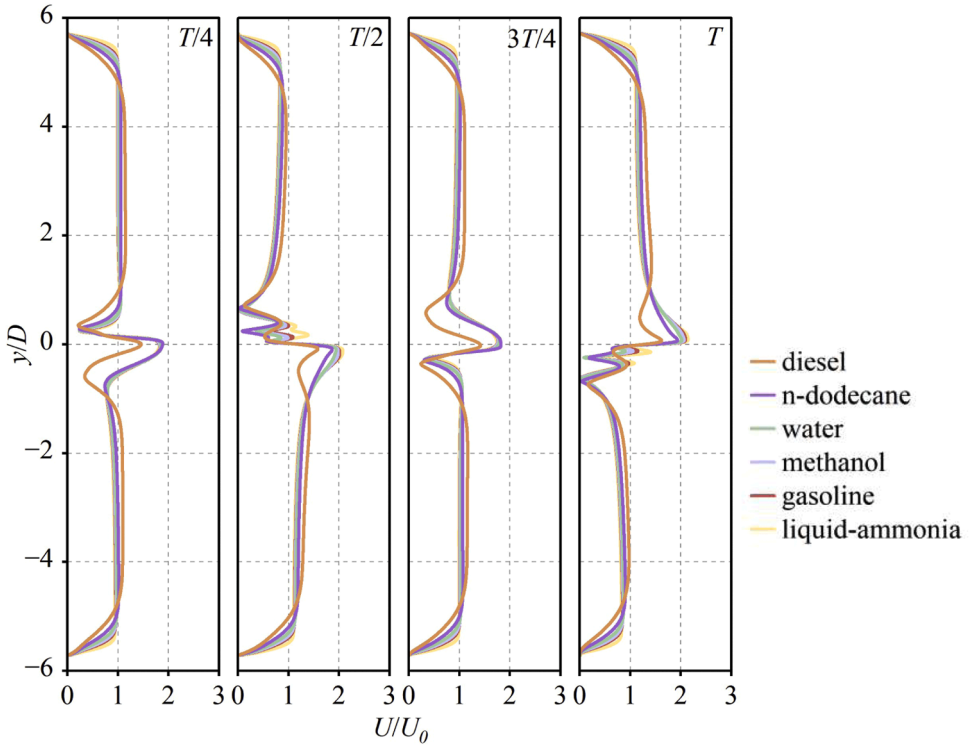


Fig. 17. The velocity distribution at $x = 12D$ under different fluids.

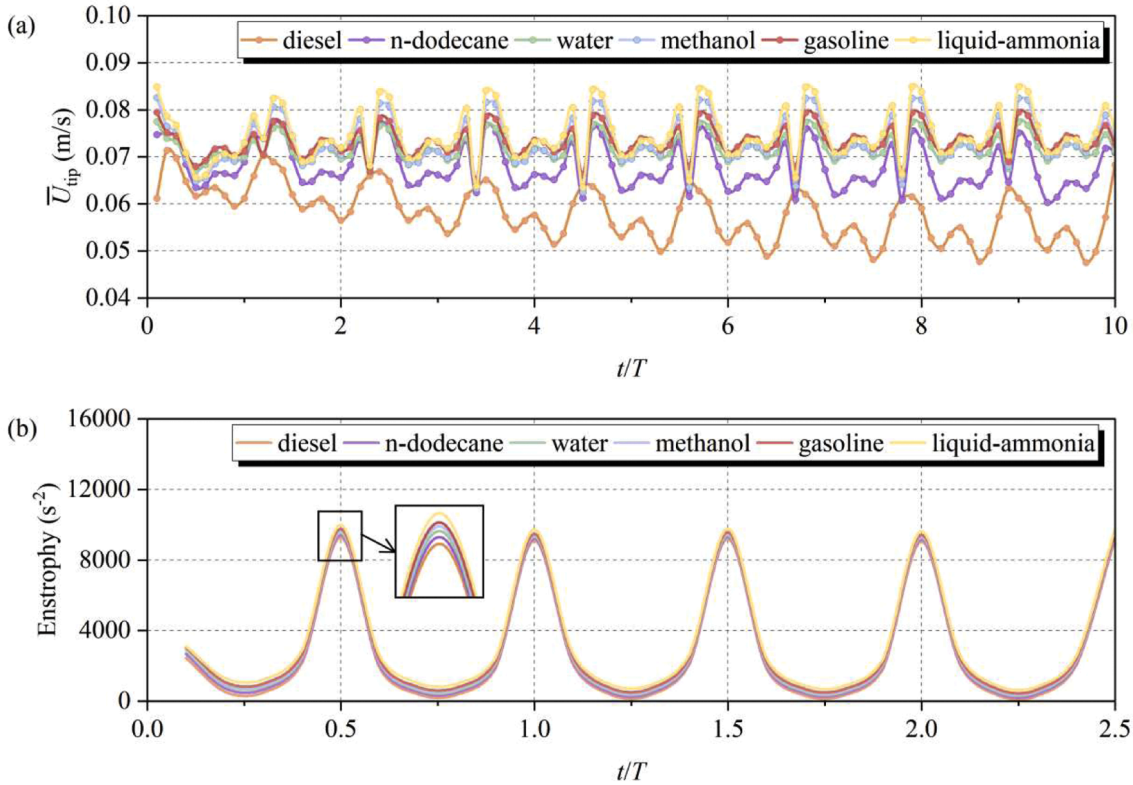


Fig. 18. Temporal evolution of (a) the near-tip spatially averaged velocity and (b) the domain-averaged enstrophy for different fluids.

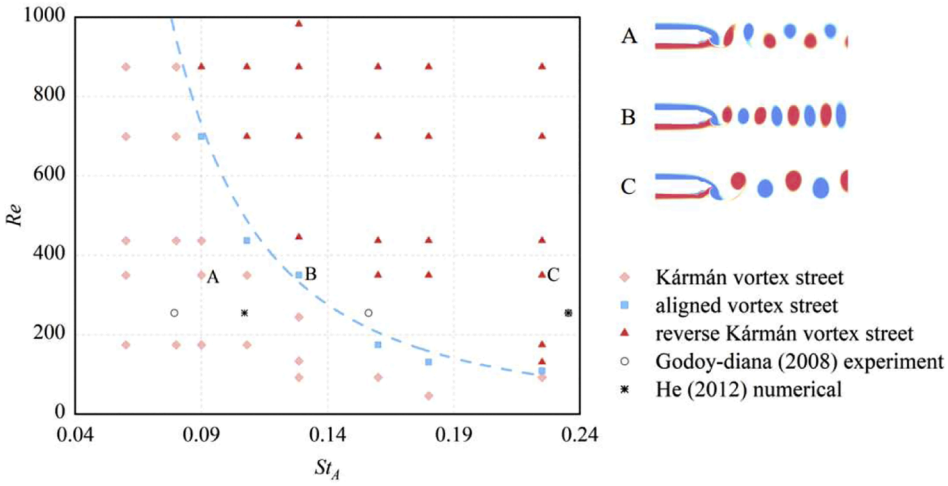


Fig. 19. Wake pattern transition diagram in the Re-St_A plane.

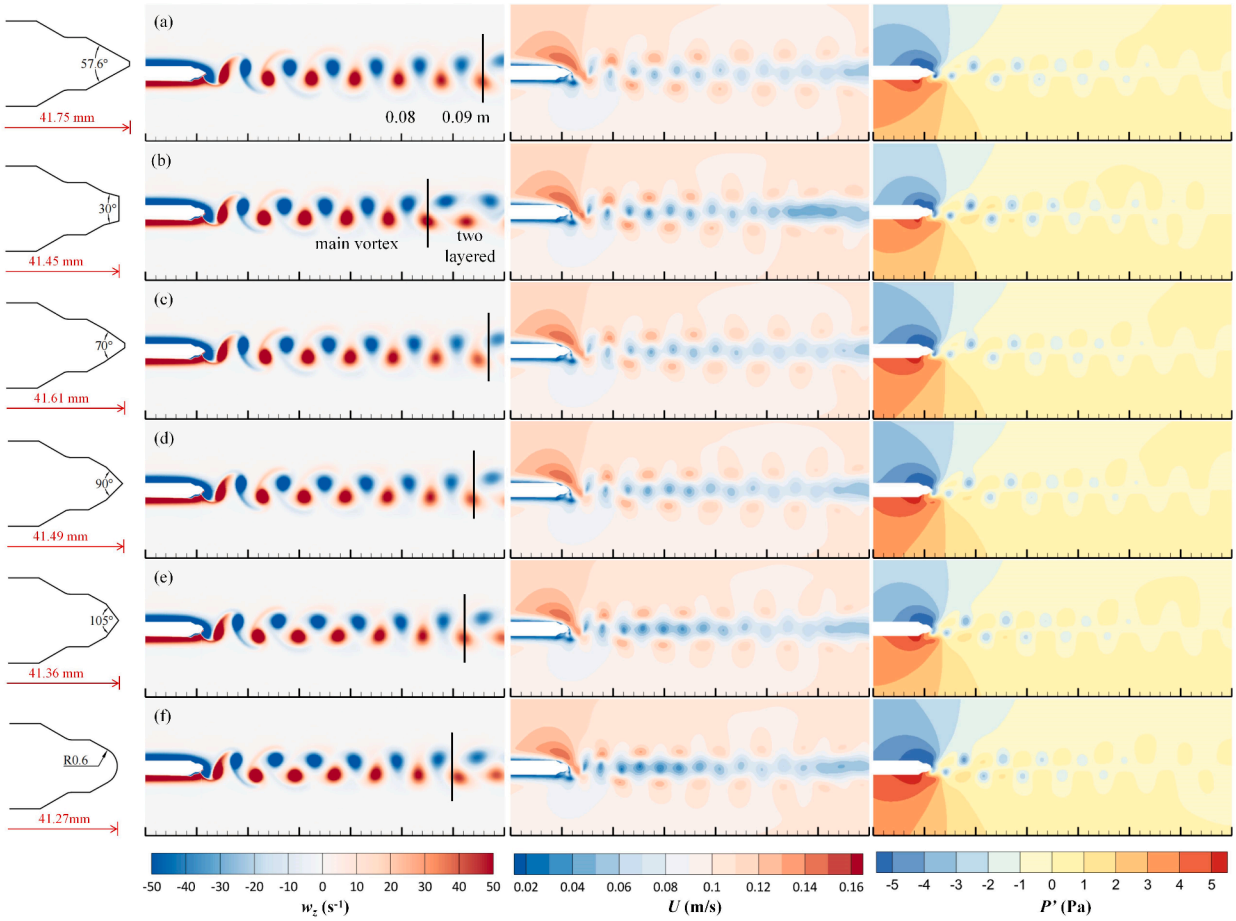


Fig. 20. Contours of vorticity, velocity, and pressure fluctuation for different needle-tip geometries: (a) shape 0; (b) shape 1; (c) shape 2; (d) shape 3; (e) shape 4; and (f) shape 5. From left to right, the columns show vorticity (s^{-1}), velocity (m/s), and pressure fluctuation (Pa), respectively.

Table 3
Relative deviations of the transition locations for different tip shapes with respect to shape 0.

Tip shape	Shape 0	Shape 1	Shape 2	Shape 3	Shape 4	Shape 5
Relative deviation (%)	0	13.54	1.04	2.08	4.17	6.25

variation in tip geometry does not fundamentally alter the formation of the oscillation-induced alternating wake. Instead, its primary effects are reflected in the vortex strength, spatial evolution, and downstream persistence.

The black lines in Fig. 20 indicate the approximate transition locations from the main-vortex region to the downstream two-layered wake, as identified from the velocity fields. Taking shape 0, the standard tip geometry used in this study, as the reference, the relative deviations of the transition locations for the other tip shapes were calculated, with the results summarized in Table 3. The relatively small deviations for most shapes suggest that the selected baseline tip geometry is reasonably representative. The transition locations vary among the six shapes, indicating that tip geometry affects the persistence and spatial evolution of the primary vortices, while the Kármán-type wake pattern remains unchanged.

To quantify the geometric effects identified qualitatively in Fig. 20, the instantaneous vorticity, velocity, and pressure fluctuation profiles were extracted along the streamwise centerline (see Fig. 21), with the streamwise coordinate normalized as $(x-x_{\mathrm{tip}})/D$. These profiles exhibit larger geometric dependence near the tip, where the local flow is most strongly influenced by tip geometry. Variations in tip angle, truncation, and curvature modify the local separation behavior and shear-layer development, thereby producing different near-tip vorticity levels. As these structures are convected downstream, viscous diffusion and vortex interactions progressively attenuate the differences introduced by the local geometry, and the amplitude differences generally become less pronounced.

These profiles also exhibit a clear streamwise phase shift, which reflects differences in vortex formation and convection. Different separation conditions can alter the distance and time required for the separated shear layers to roll up into vortices, while small differences in vortex convection velocity may further increase the downstream phase offset. Shape 1 exhibits strong near-tip response in all three quantities, likely owing to its wider terminal flat and greater local bluntness.

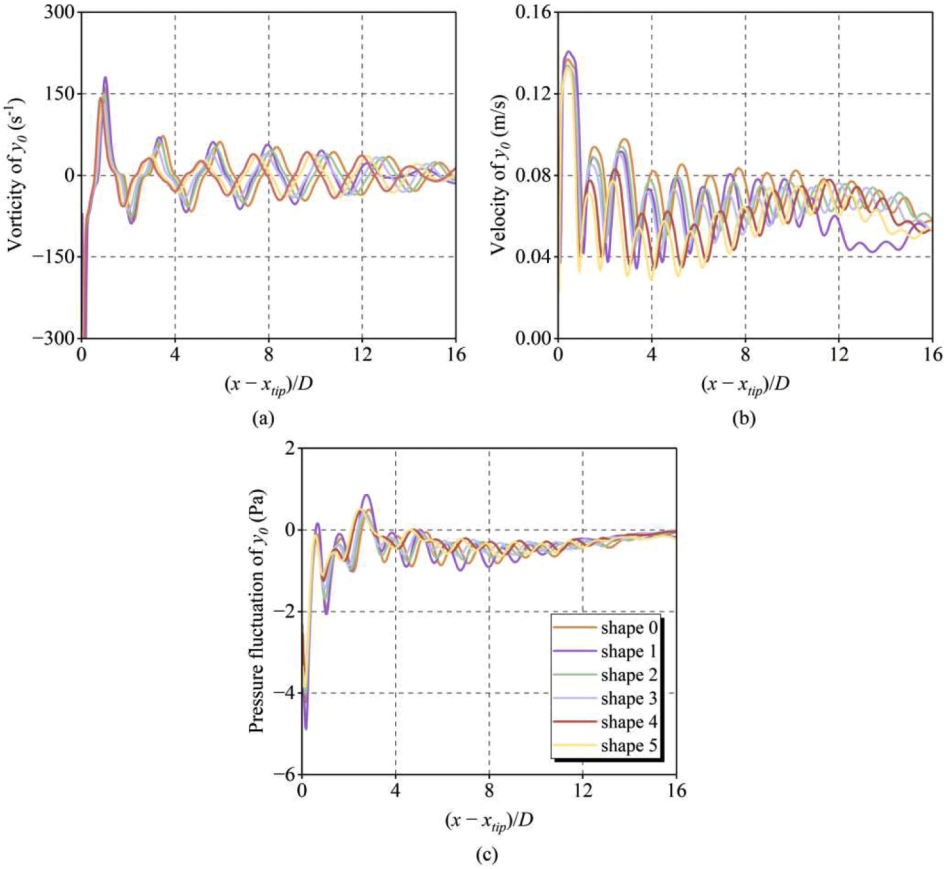


Fig. 21. Streamwise centerline profiles of (a) vorticity, (b) velocity, and (c) pressure fluctuation for different tip geometries.

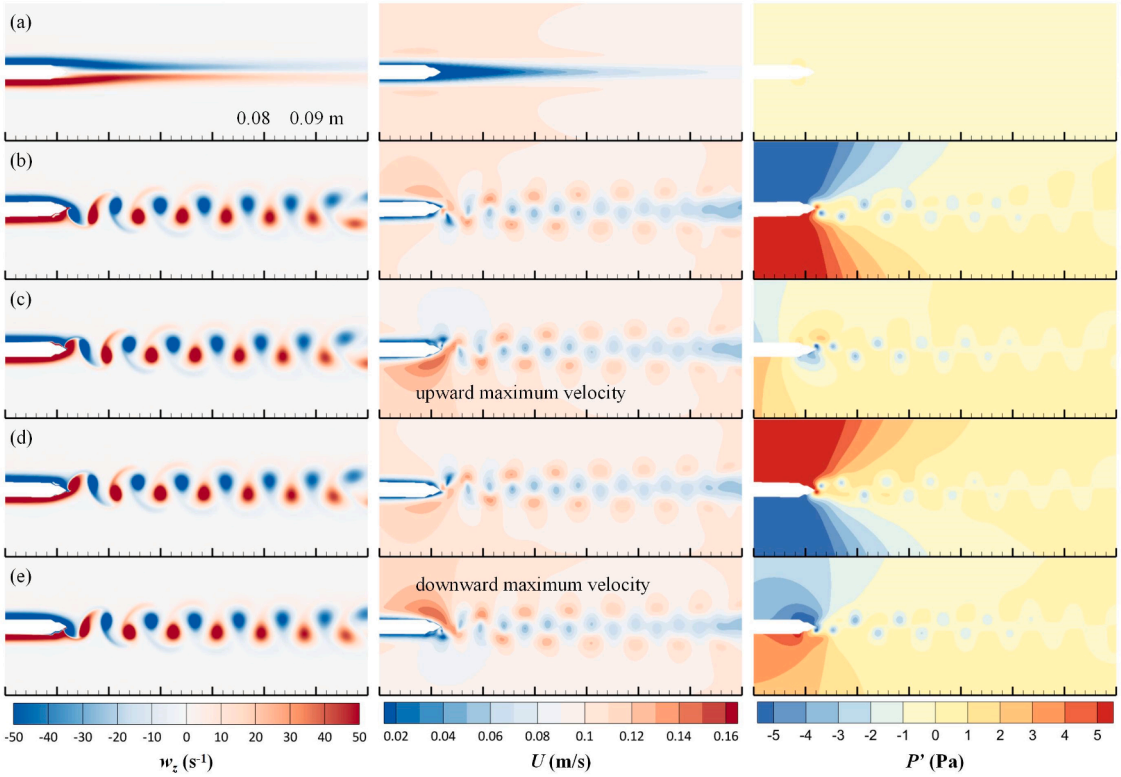


Fig. 22. Comparison of the stationary wake and phase-resolved wake evolution over one oscillation cycle in terms of vorticity, velocity, and pressure fluctuation: (a) stationary needle; (b) $T/4$, upper extreme position; (c) $T/2$, center position; (d) $3T/4$, lower extreme position; and (e) T, center position. From left to right, the columns show vorticity (s^{-1}), velocity (m/s), and pressure fluctuation (Pa), respectively.

3.3.2. Physical mechanism of vortex generation around the needle tip

The phase-resolved flow fields in Fig. 22, obtained at $A = 0.45$ mm, $f = 10$ Hz, and $U_0 = 0.1$ m/s, provide further insight into the vortex-generation mechanism. The incoming flow is approximately parallel to the needle axis and develops along the needle surfaces before reaching the downstream tip. Together with the absence of pronounced alternating vortex formation for the stationary needle (Fig. 22(a)), this indicates that the observed wake is not simply conventional self-sustained Kármán shedding from a stationary bluff body in cross-flow.

In the stationary case, boundary-layer vorticity of opposite sign develops along the upper and lower needle surfaces and is carried beyond the tip into two approximately symmetric shear layers. These layers do not develop into the pronounced alternating vortices observed during needle oscillation. The tip geometry therefore primarily influences the initial shear-layer conditions, including their strength, thickness, and near-wake development, rather than determining the alternating wake pattern itself.

In the classical description of wake formation, large-scale vortices develop through the accumulation, interaction, and roll-up of vorticity carried by separated shear layers [41]. In the present system, transverse oscillation introduces periodic transverse relative motion between the needle and the surrounding fluid, which breaks the upper-lower symmetry of the near-tip flow and modifies the local velocity and pressure distributions. This periodic forcing organizes the shear-layer roll-up into alternating coherent vortices, consistent with previous studies showing that imposed body motion can control the timing and phase of shear-layer roll-up and vortex formation [42].

The sequence in Fig. 22(b)–(e) illustrates this process over one oscillation cycle. Once the upper-lower symmetry is disturbed, one shear layer is preferentially strengthened and rolls up into a coherent primary vortex. As the needle reverses direction, this vortex is convected downstream while the opposite-sign shear layer is strengthened and forms the next vortex. The process is repeated approximately every half-cycle, producing the alternating positive- and negative-vorticity structures observed downstream. The velocity and pressure-fluctuation fields provide complementary evidence, with each near-tip vortex accompanied by localized velocity and pressure redistribution and a reversal of the upper-lower asymmetry as the needle motion reverses. Because shear-layer development and vortex roll-up require a finite time, the wake response lags the instantaneous needle motion. Consequently, developing vortices can remain present at the extreme needle positions, where the instantaneous transverse velocity of the needle is zero.

The present mechanism differs from those reported for oscillating foils, particularly combined pitching-heaving configurations, where leading- and trailing-edge vortex interactions can play a key role in wake deflection, jet-switching, and aperiodic transitions [11,12,36]. Here, the incoming flow is approximately aligned with the needle axis, and the stationary-needle calculation produces two nearly symmetric shear layers without pronounced alternating shedding. The alternating wake is therefore attributed to the periodic

upper-lower asymmetry imposed on the tip shear layers by transverse bending motion, rather than to a conventional foil-type leading-edge-vortex mechanism.

Thus, tip geometry influences the initial shear-layer conditions, whereas transverse oscillation provides the periodic forcing that organizes their alternating roll-up and downstream convection. Under the present conditions, the alternating wake therefore arises from oscillation-modulated shear-layer dynamics rather than conventional self-sustained shedding from a stationary bluff body.

3.3.3. *Evolution of hydrodynamic forces*

Previous studies have shown that the wake evolution generates unsteady hydrodynamic forces on the needle body, which may affect the oscillation characteristics. Investigating these unsteady hydrodynamic forces is therefore important for understanding the oscillation characteristics of the needle and the associated fluid-structure interaction mechanisms. Accordingly, the streamwise (*X*-direction) and transverse (*Y*-direction) forces were quantitatively analyzed over variations in oscillation amplitude, frequency, inflow velocity, and fluid properties.

The transient force data obtained from numerical simulations are presented in Figs. 23 and 24. Spline curves were used only for trend visualization, whereas all quantitative analyses were based on the original simulation data.

(i) Transverse Force.

Periodic fluid disturbances in the near-needle region induce dynamic loads on the needle body, manifesting primarily as fluctuating transverse forces. The transverse force exhibits a periodic variation at a frequency that coincides with the vortex shedding frequency [43]. As shown in Fig. 23(a-c), the fluctuation amplitude of these forces increases with the oscillation amplitude, frequency, and inflow velocity. The comparison among the tested fluids further suggests that the transverse-force fluctuation is more strongly influenced by fluid density than by viscosity (Fig. 23(d)). The transverse force (F_y) can be expressed as:

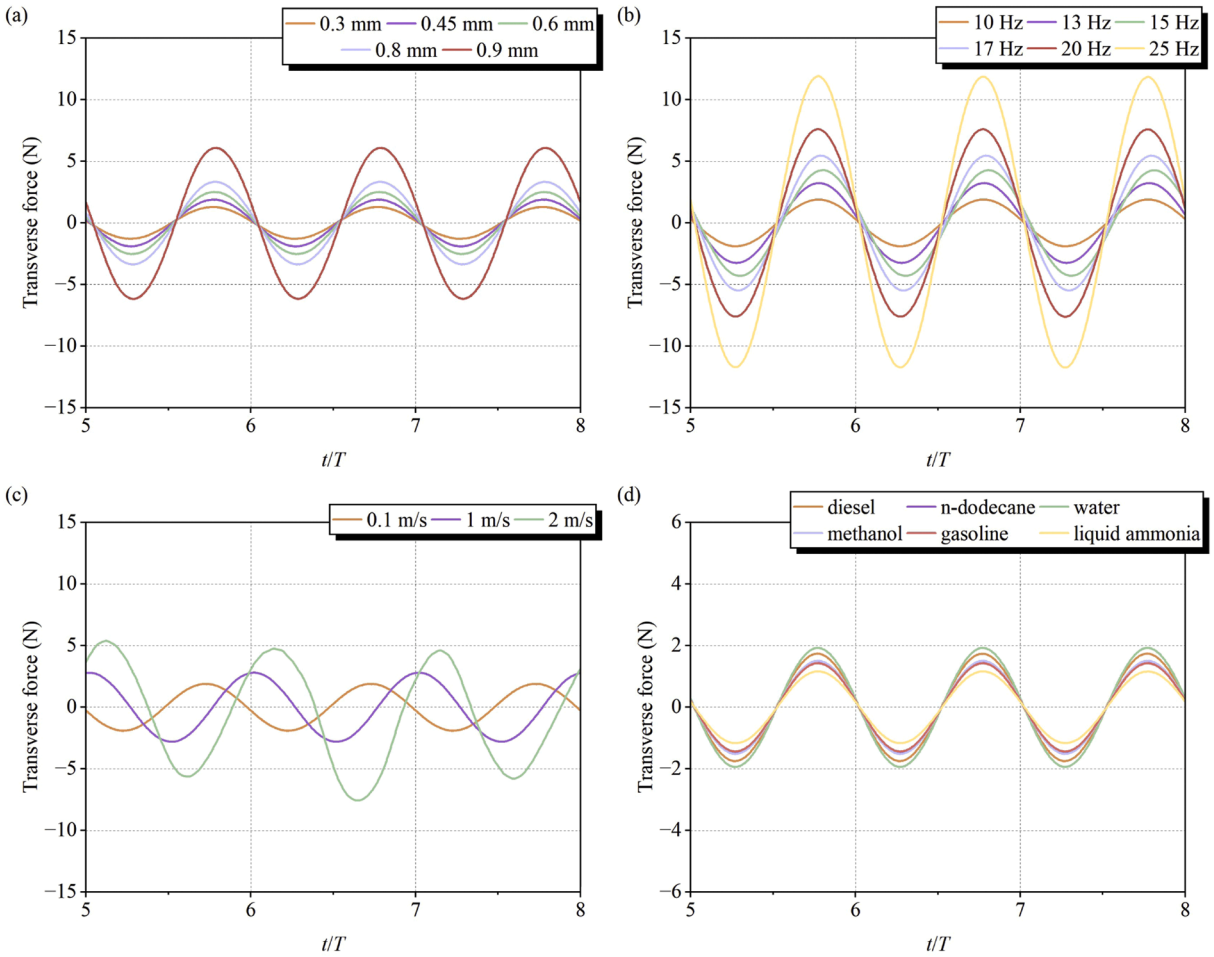


Fig. 23. The transverse force under different conditions: (a) amplitudes; (b) frequencies; (c) inflow velocities; and (d) fluids.

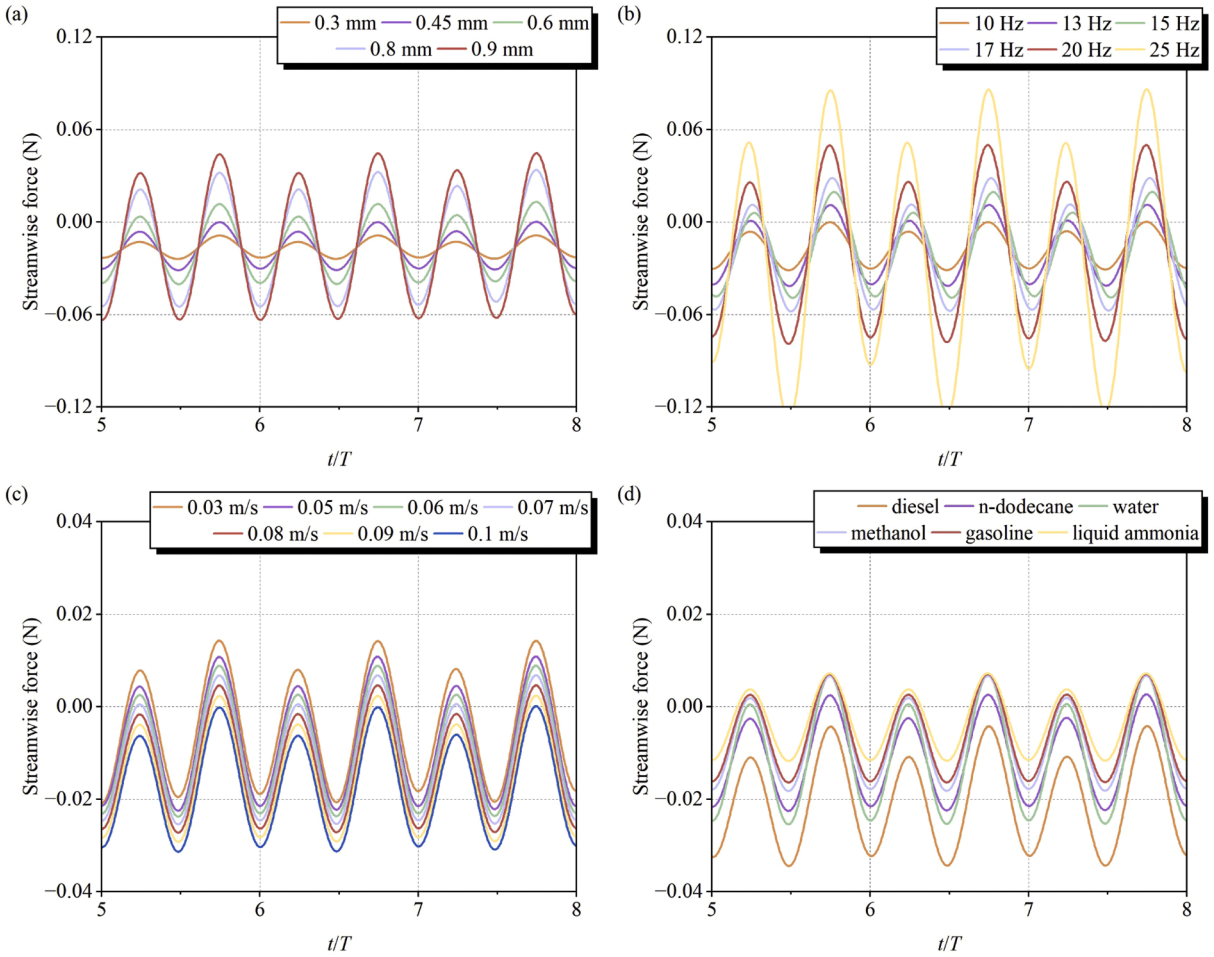


Fig. 24. The streamwise force under different conditions: (a) amplitudes; (b) frequencies; (c) inflow velocities; and (d) fluids.

$$F_y = \frac{1}{2}\rho U^2 S_{ref} C_L \tag{17}$$

where S_{ref} is the characteristic reference area used in the definition of the transverse force coefficient, and C_L is the transverse force coefficient.

Density directly enters the dynamic-pressure scaling of the force, whereas viscosity affects C_L through its influence on the *Re* and the associated flow dynamics. Consistent with this behavior, in Fig. 23(d), fluids with comparable densities (methanol, n-dodecane, and gasoline) exhibit similar transverse-force fluctuation profiles despite differences in viscosity.

In Fig. 23(c), increasing inflow velocity also introduces a noticeable phase shift in F_y. The associated increase in *Re* modifies the near-tip shear-layer dynamics and vortex formation and convection, thereby altering the timing of the transverse-force response. The significance of this force–motion phase relationship for hydrodynamic damping and stability is examined in the following section.

(ii) Transverse Hydrodynamic Damping

As discussed in the previous section, the increasing inflow velocity introduces a noticeable phase shift in the transverse force relative to the prescribed needle motion. Because the oscillation amplitude and frequency remain unchanged, the needle displacement and velocity histories are identical for all inflow velocities. Differences in the cycle-integrated fluid work therefore directly reflect changes in the hydrodynamic force response, particularly its magnitude and phase relative to the needle velocity.

To evaluate the hydrodynamic contribution to the needle oscillation, an equivalent hydrodynamic damping coefficient (C_{added}) was determined from the work performed by the transverse fluid force over one oscillation cycle. The prescribed transverse displacement and velocity of the needle are

$$y(t) = A\sin(\omega t) \tag{18}$$

and

$$\dot{y}(t) = A\omega\cos(\omega t) \tag{19}$$

$$\omega = 2\pi f \tag{20}$$

where $A = 0.45$ mm and $f = 10$ Hz.

The work performed by the transverse fluid force over one oscillation cycle is

$$W = \int_{t_0}^{t_0+T} F_y(t)\dot{y}(t)\mathrm{d}t \tag{21}$$

where $F_y(t)$ denotes the transverse force exerted by the fluid on the needle. To minimize the effects of the initial transient and any non-synchronous vortex-shedding components, the work per cycle was evaluated after the flow had reached a statistically periodic state and was averaged over several consecutive oscillation cycles.

An equivalent transverse hydrodynamic damping coefficient is defined as

$$C_{\text{added}} = -\frac{W}{\pi\omega A^2} \tag{22}$$

According to this definition, $C_{\text{added}} > 0$ indicates that the fluid removes energy from the needle motion and therefore provides a stabilizing contribution. In contrast, $C_{\text{added}} < 0$ indicates that the fluid supplies energy to the needle motion and therefore provides a destabilizing contribution.

The importance of the force-motion phase and cycle-integrated fluid work is consistent with energy-based analyses of flow-induced and semi-passive foil oscillations, for which the direction and magnitude of fluid-structure energy transfer govern oscillation growth, saturation, and performance [14,15]. In the present prescribed-motion framework, the equivalent damping coefficient should be interpreted as a diagnostic of the hydrodynamic contribution rather than as a prediction of the freely coupled needle response. Nevertheless, the sign reversal identifies an inflow-velocity-dependent change in the tendency of the fluid to remove energy from, or supply energy to, the transverse needle motion.

The calculated cycle-averaged work and equivalent transverse hydrodynamic damping coefficients are summarized in Table 4. At an inflow velocity of 0.1 m/s, the fluid performs negative work on the needle over one oscillation cycle, resulting in a positive hydrodynamic damping coefficient of 9.46 N·s/m^2. This result indicates that the fluid removes energy from the prescribed needle motion and provides a stabilizing contribution. At $U_0 = 1$ and 2 m/s, the work becomes positive and C_{added} decreases to − 98.7 and − 131.6 N·s/m^2, respectively, indicating increasing net energy transfer from the fluid to the prescribed transverse motion. For a freely responding needle, such negative hydrodynamic damping would promote oscillation growth and could contribute to instability if it exceeds the positive structural and other dissipative damping.

(iii) Streamwise Force

The fluctuation of the streamwise force (F_x) is significantly smaller than that of the transverse force, while its fluctuation frequency is approximately twice the transverse-force frequency [44]. The streamwise force results from the combined pressure and viscous stresses acting on the needle surface. The alternating vortex shedding of upper and lower sides induces two streamwise force fluctuations per oscillation cycle. Because the wake evolution is synchronized with the prescribed oscillation, the dominant F_x frequency increases proportionally with the oscillation frequency.

Differences in fluid viscosity modify the viscous shear stresses acting on the needle surface and can therefore affect the streamwise-force response. Among the fluids considered, the relatively high viscosity of diesel is associated with a larger streamwise-force fluctuation amplitude, whereas the lower viscosity of liquid ammonia corresponds to a smaller fluctuation (Fig. 24(d)).

When the needle approaches its maximum transverse displacement, its streamwise force reaches a peak regardless of the deflection direction. At these extreme positions, the bending deformation and local inclination of the needle are greatest. The resulting increase in the projected frontal area normal to the incoming flow enhances the form-drag contribution to the streamwise force.

As the needle passes through the equilibrium position, the transverse velocity reaches its maximum, while the projected area becomes minimal and the form drag declines sharply. The superposition of the transverse and the freestream velocity leads to an effective angle of attack, giving rise to a thrust-like effect. At this time, the resultant force opposite to the incoming flow reaches a trough. The magnitude of the streamwise force is determined by the competition among form drag, friction drag, and wake-induced

Table 4
Added hydrodynamic damping coefficients at varying inflow velocities.

Inflow velocity U_0 (m/s)	Mean fluid work per cycle W (J/m)	Added Damping C_{added} (N·s/m^2)	Hydrodynamic contribution
0.1	-3.78×10^{-4}	9.46	Energy dissipation; stabilizing
1	3.95×10^{-3}	− 98.7	Energy input; destabilizing
2	5.26×10^{-3}	− 131.6	Energy input; destabilizing

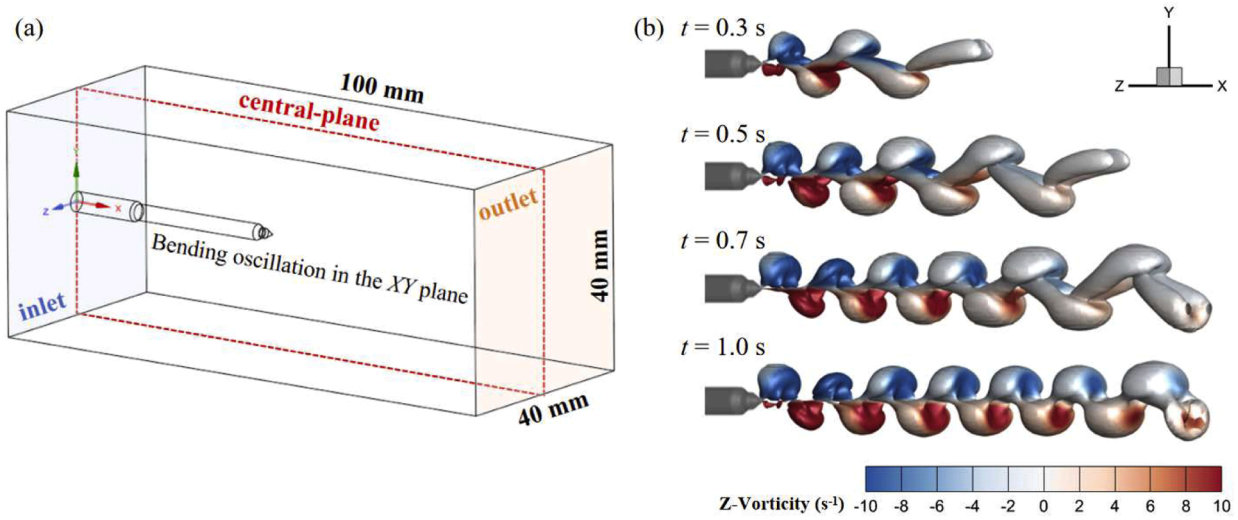


Fig. 25. Three-dimensional simulation of the oscillating needle and its wake dynamics: (a) three-dimensional computational model and (b) evolution of the wake vortical structures. The prescribed bending oscillation of the needle is restricted to the *XY* plane. The instantaneous vortical structures are identified using the Ω-criterion (Ω = 0.52) [45,46] and colored by the *z*-vorticity.

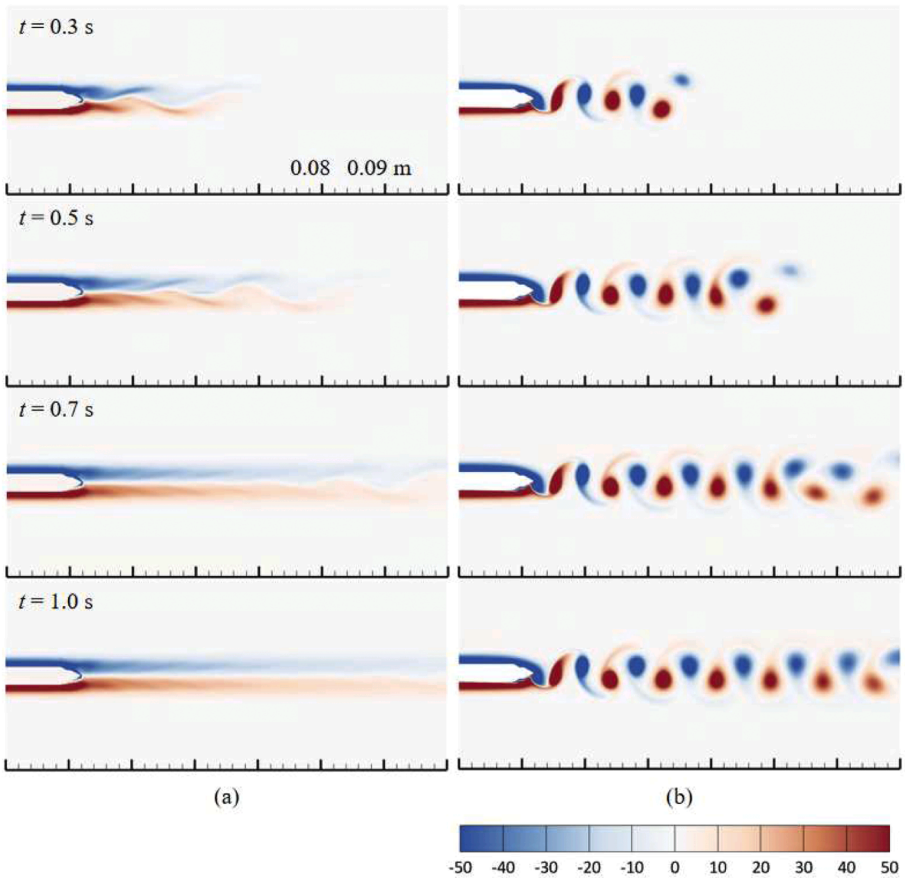


Fig. 26. Comparison of the *z*-vorticity distributions between the 3D and 2D simulations: (a) central-plane results ($z = 0$) from the 3D simulation; (b) corresponding results from the 2D simulation.

thrust.

3.4. Assessment of three-dimensional effects and applicability of the two-dimensional model

To assess the influence of the 2D assumption, an additional 3D simulation was performed for the baseline condition of $f = 10$ Hz, $A = 0.45$ mm, and $U_0 = 0.1$ m/s, using the same needle geometry and operating conditions as in the corresponding 2D case. The 3D computational model is shown in Fig. 25(a), while instantaneous vortical structures at selected instants are presented in Fig. 25(b).

As the wake develops downstream, alternating hairpin-like vortical structures form behind the needle tip. Although the 3D vortices exhibit pronounced spatial deformation compared with the compact vortices in the 2D simulation, their large-scale alternating arrangement remains qualitatively consistent. The comparable downstream extent of the wake also suggests similar streamwise convection characteristics. These results indicate that, although the 2D model cannot reproduce the detailed 3D vortex topology, it can still capture the main wake organization and evolution.

Fig. 26 further compares the z-vorticity distributions on the central plane ($z = 0$) of the 3D simulation with those obtained from the 2D simulation. The 2D wake is characterized by compact and well-separated alternating vortices, whereas the central-plane vorticity in the 3D simulation is mainly distributed in diffuse and elongated shear-layer-like structures. This difference reflects the pronounced 3D deformation and spatial redistribution of the vortical structures. Therefore, a single central-plane section cannot fully represent the 3D wake topology. Nevertheless, the 2D simulation retains the large-scale alternating wake organization observed in the full 3D vortex structures.

The force responses show a similar trend, as shown in Fig. 27. For consistency, the reference depth in the 2D simulation was set to 40 mm, equal to that of the 3D model. Although the 3D simulation predicts a lower transverse force, the overall periodic response remains qualitatively consistent with the 2D result. This indicates that the 2D model is suitable for identifying qualitative wake characteristics and parametric trends, although it cannot fully reproduce the detailed features of the 3D flow.

The sensitivity of oscillating-body wakes to three-dimensionality is also emphasized in previous 2D fluid-structure interaction (FSI) studies. Depending on kinematics and aspect ratio, spanwise perturbations and tip-vortex effects can invalidate a direct quantitative extension of 2D wake structures, particularly for low-amplitude/high-frequency motion or low-aspect-ratio configurations [11,12]. Similar limitations have also been reported for 2D low-*Re* flow-induced-oscillation models [14]. The present 3D baseline comparison is consistent with these observations, further indicating that the 2D model is more reliable for identifying qualitative wake characteristics and parametric trends than for reproducing all details of the 3D flow.

4. Conclusion

Experimental results demonstrate that needle oscillation can generate alternating vortical wakes. Building on these observations, the present CFD study systematically investigates the effects of oscillation parameters and fluid properties on wake morphology and vortex dynamics, and further examines the associated hydrodynamic forces and damping. The sensitivities of the wake to needle-tip geometry and bending-oscillation mode are also assessed, as well as the influence of 3D effects on the applicability of the 2D model. The main conclusions are summarized as follows:

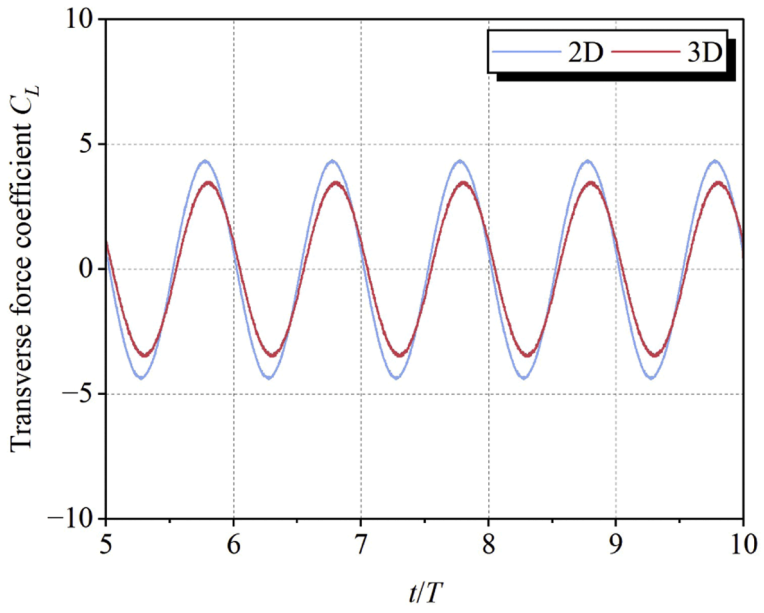


Fig. 27. Comparison of the transverse force coefficient C_L.

(i) Increasing the oscillation amplitude and frequency strengthens the near-tip velocity gradients and vorticity, leading to higher global enstrophy. As the St_A increases, the enhanced transverse forcing strengthens the lateral deflection and alternating roll-up of the shear layers, thereby reorganizing the spatial arrangement of the shed vortices and driving the wake from a Kármán-type to a reverse-Kármán-type pattern.

(ii) The inflow velocity and fluid properties significantly influence wake characteristics. Increasing the inflow velocity reduces the relative strength of transverse forcing, while higher viscosity enhances vorticity diffusion and attenuates oscillation-induced disturbances. These effects reduce the lateral displacement of the forming vortices and drive the wake from a reverse-Kármán-type toward a Kármán-type arrangement. Meanwhile, the streamwise vortex spacing increases with inflow velocity.

(iii) The wake transition is governed by the combined effects of oscillation parameters, inflow velocity, and fluid properties. These effects can be characterized by Re and St_A, which jointly dictate the wake modes. The transition boundaries exhibit a power-law relationship in the St_A-Re regime map. Specifically, increasing Re reduces the critical St_A required for wake transition, whereas lower Re demands a correspondingly higher St_A.

(iv) The oscillation-induced wake generates forces on the needle, with transverse-force fluctuations substantially exceeding those in the streamwise direction. The streamwise force exhibits a dominant frequency approximately twice that of the transverse force. Increasing inflow velocity not only amplifies the transverse-force response but also alters its phase relative to the needle motion, changing the net fluid-structure energy transfer. As a result, the transverse hydrodynamic damping changes from positive at low inflow velocity to negative at higher velocities, indicating a transition from a stabilizing to a destabilizing hydrodynamic contribution.

(v) The alternating wake is generated by oscillation-induced asymmetric roll-up of the shear layers, whereas a stationary needle produces approximately symmetric shear layers without pronounced alternating vortices. Variations in needle-tip geometry and bending-oscillation mode do not fundamentally alter this wake pattern, but slightly modify its quantitative characteristics and downstream evolution.

(vi) The 3D simulation shows alternating hairpin-like vortical structures. Their large-scale organization and downstream evolution remain qualitatively consistent with the 2D results, despite differences in the detailed vortex topology. A lower transverse force amplitude is predicted in 3D, while a similar force-motion phase relationship is retained. Thus, the 2D model can capture the main wake characteristics and parametric trends, but does not fully reproduce the detailed 3D flow and loading features.

CRediT authorship contribution statement

Ziman Wang: Supervision, Methodology, Conceptualization. **Tong Liang:** Writing – original draft, Investigation, Formal analysis. **Changzhao Jiang:** Writing – review & editing, Conceptualization. **Yuanhao Yin:** Software, Data curation. **Xiaohu Gu:** Visualization, Investigation. **Heping Xiang:** Visualization, Funding acquisition. **Yingjie Chen:** Visualization, Resources. **Yan Cao:** Resources, Funding acquisition.

Declaration of competing interest

The authors declare that they have no known competing financial interests or personal relationships that could have appeared to influence the work reported in this paper.

Acknowledgements

This research did not receive any specific grant from funding agencies in the public, commercial, or not-for-profit sectors.

Appendix A. Sensitivity to the Prescribed Needle Bending Profile

To assess the sensitivity of the predicted wake dynamics to the prescribed spatial deformation of the needle, additional simulations were performed using the first bending-mode shape of an ideal Euler-Bernoulli cantilever beam as an alternative deformation profile. The normalized mode shape is expressed as

$$\Phi_1(x) = \frac{\phi_1(x)}{\phi_1(L)}, \tag{A.1}$$

with

$$\phi_1(x) = \cosh(\beta_1 x) - \cos(\beta_1 x) - \sigma_1[\sinh(\beta_1 x) - \sin(\beta_1 x)], \tag{A.2}$$

where

$$\beta_1 L = 1.875104 \tag{A.3}$$

and

$$\sigma_1 = \frac{\cosh(\beta_1 L) + \cos(\beta_1 L)}{\sinh(\beta_1 L) + \sin(\beta_1 L)}. \tag{A.4}$$

Here, L is the effective cantilever length measured from the fixed end to the needle tip. The first-mode deformation was prescribed as

$$w(x,t) = A\Phi_1(x)\sin(2\pi ft), \tag{A.5}$$

so that

$$\Phi_1(x) = 1 \tag{A.6}$$

and hence

$$w(x,t) = A\sin(2\pi ft). \tag{A.7}$$

Therefore, the circular-arc and first-mode calculations have identical needle-tip amplitude, frequency, and phase, and differ only in the spatial distribution of the needle deformation.

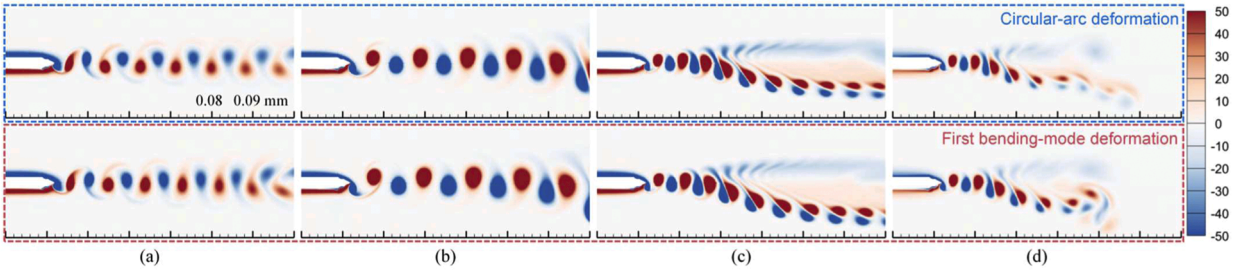


Fig. A.1. Comparison of instantaneous vorticity fields under different deformation profiles ($t = 1$ s). (a) $f = 10$ Hz, $A = 0.45$ mm, $U_0 = 0.10$ m/s; (b) $f = 10$ Hz, $A = 0.90$ mm, $U_0 = 0.10$ m/s; (c) $f = 20$ Hz, $A = 0.45$ mm, $U_0 = 0.10$ m/s; (d) $f = 10$ Hz, $A = 0.45$ mm, $U_0 = 0.05$ m/s.

Four representative operating conditions were examined, covering variations in vibration amplitude, frequency, and inflow velocity. Fig. A.1 compares the instantaneous vorticity fields obtained using the two deformation profiles. Although modest local differences in vortex strength and vortex-core position are observed, the vortex-formation process near the needle tip, the alternating shedding pattern, and the overall wake topology remain qualitatively similar.

The quantitative comparisons are summarized in Table A.1. The relative difference in the domain-averaged absolute vorticity ($|\omega_z|$) ranges from 3.63% to 8.60%, whereas that in the domain-averaged velocity magnitude is only 0.25%–1.11%. The corresponding differences in local extrema remain below 10%. In addition, the transverse hydrodynamic force histories obtained using the two deformation profiles exhibit closely similar temporal evolution with no discernible phase shift, while the relative difference in $F_{y,RMS}$ remains within 3.39%–8.36% across the four conditions.

These results show that the prescribed bending profile has a slight influence on local instantaneous quantities but does not materially alter the principal wake topology, vortex-shedding behavior, or integrated transverse hydrodynamic response. Thus, the main conclusions of the present parametric study are robust with respect to the choice of prescribed spatial bending profile.

Table A.1
Relative differences in whole-domain vorticity, velocity, and transverse force under different deformation profiles.

case	A (mm)	f (Hz)	U_0 (m/s)	Mean $\|\omega_z\|$	Max. ω_z	Min. ω_z	Mean velocity	$F_{y,\mathrm{RMS}}$
i	0.45	10	0.10	3.63%	0.04%	3.58%	0.25%	3.49%
ii	0.90	10	0.10	4.89%	8.99%	2.25%	1.11%	8.36%
iii	0.45	20	0.10	6.02%	7.32%	3.69%	0.63%	3.73%
iv	0.45	10	0.05	8.60%	9.00%	9.92%	0.57%	3.39%

Appendix B. Sensitivity to the Transverse Domain-Width

To assess the influence of the lateral boundaries, the transverse computational-domain width was increased from 11.4D to 21D while maintaining the same wall boundary conditions and numerical settings. Two representative conditions were examined: (i) $A = 0.90$ mm, $f = 10$ Hz and (ii) $A = 0.45$ mm, $f = 25$ Hz, both at $U_0 = 0.10$ m/s.

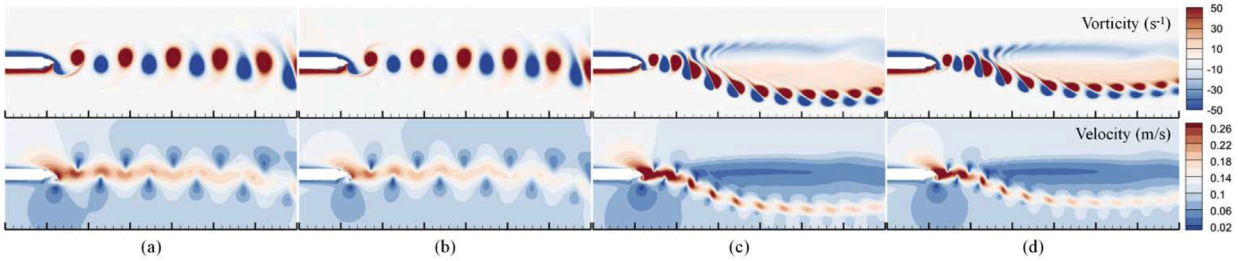


Fig. B.1. Comparison of instantaneous vorticity and velocity distributions at $t = 1$ s for different transverse domain widths: (a) width = 11.4*D*, $A = 0.90$ mm, $f = 10$ Hz; (b) width = 21*D*, $A = 0.90$ mm, $f = 10$ Hz; (c) width = 11.4*D*, $A = 0.45$ mm, $f = 25$ Hz; and (d) width = 21*D*, $A = 0.45$ mm, $f = 25$ Hz.

As shown in Fig. B.1, the vorticity and velocity distributions at $t = 1$ s exhibit similar wake structures for both widths. The quantitative comparisons in Table B.1 show that the relative differences in mean velocity are below 1%. Although certain quantitative differences are observed, the principal wake structures and overall flow characteristics remain largely consistent between the two domain widths. These results indicate that the original 11.4*D* domain is sufficient to capture the principal wake structures and overall flow trends investigated in this study, although moderate quantitative sensitivity remains in some flow quantities.

Table B.1
Relative differences in representative flow quantities between the transverse domain widths of 11.4*D* and 21*D*.

A (mm)	f (Hz)	U_0 (m/s)	Mean $\lvert\omega_z\rvert$	Max. ω_z	Min. ω_z	Mean velocity	$F_{y,\mathrm{RMS}}$
0.90	10	0.10	7.07%	9.85%	5.09%	0.79%	6.49%
0.45	25	0.10	6.54%	3.96%	8.32%	0.45%	6.48%

Appendix C. Additional validation at Re = 1000

To further evaluate the applicability of the numerical framework at Reynolds numbers approaching the upper end of the range considered in the present study, an additional benchmark simulation was conducted for 2D unsteady flow past a stationary circular cylinder at $Re = 1000$. The simulation was performed using the same numerical methodology adopted throughout the present study and was compared against published 2D DNS data from Ref. [40]. The DNS data were taken as a high-fidelity reference solution. As shown in Fig. C.1, both results exhibit the characteristic alternating vortex shedding downstream of the cylinder, with comparable near-wake vortex organization and shear-layer development.

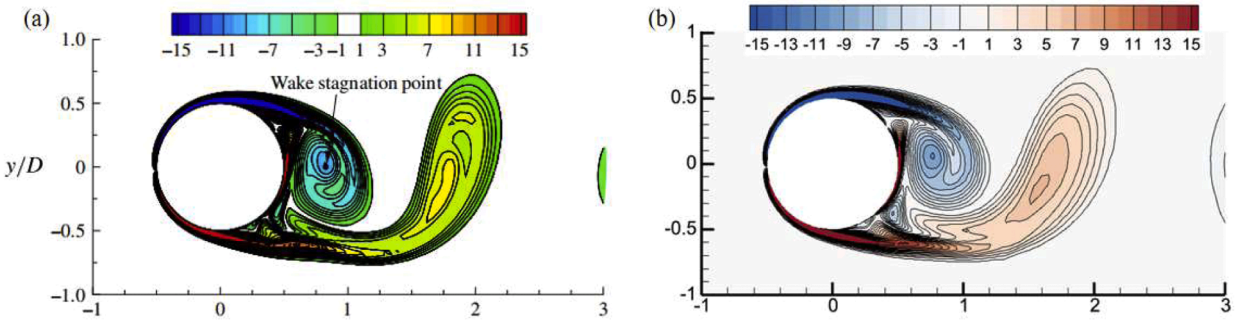


Fig. C.1. Comparison of instantaneous vorticity contours for flow past a circular cylinder at $Re = 1000$: (a) 2D DNS result [40]; (b) present numerical result.

Unlike the forced-oscillation cases considered in the previous comparisons, the vortex-shedding frequency was not prescribed in this benchmark. Instead, periodic vortex shedding developed naturally from the transient flow solution. After the flow reached a statistically periodic state, the lift and drag coefficients were monitored over multiple shedding cycles.

The instantaneous drag and lift coefficients are defined as

$$C_D = \frac{F_D}{\frac{1}{2}\rho U^2 D} \tag{C.1}$$

$$C_L = \frac{F_L}{\frac{1}{2}\rho U^2 D} \tag{C.2}$$

respectively, where F_D and F_L denote the drag and lift forces per unit span acting on the cylinder.

The time-averaged drag coefficient ($\overline{C_D}$) was calculated over the statistically periodic portion of the solution as

$$\overline{C_D} = \frac{1}{N}\sum_{i=1}^{N} C_{D,i} \tag{C.3}$$

where N is the number of sampled values. The lift-fluctuation coefficient ($C_L^{'}$) was evaluated using the root-mean-square definition [40]:

$$C_L^{'} = \sqrt{\frac{1}{N}\sum_{i=1}^{N}\left(C_{L,i} - \overline{C_L}\right)^2}. \tag{C.4}$$

Table C.1
Comparison of the present numerical results with the 2D DNS results [40] at $Re = 1000$.

Re	Quantity	Jiang & Cheng (2017), 2D DNS	Present study	Relative error
1000	St	0.2377	0.2316	2.566%
1000	$\overline{C_D}$	1.513	1.470	2.842%
1000	$C_L^{'}$	1.031	0.953	7.565%

The Strouhal number was determined from the dominant frequency (f_s) of the lift-coefficient signal according to $St = f_s D/U$. Table C.1 compares the present predictions with the DNS results. Good agreement is obtained for the Strouhal number, mean drag coefficient, and lift-fluctuation coefficient, indicating that the numerical framework accurately captures the principal unsteady wake characteristics at $Re = 1000$.

Data availability

Data will be made available on request.

References

[1] W. Huang, S. Moon, Y. Gao, Z. Li, J. Wang, Eccentric needle motion effect on near-nozzle dynamics of diesel spray, Fuel 206 (2017) 409–419, https://doi.org/10.1016/j.fuel.2017.06.012.

[2] F. Liu, Z. Li, Z. Wang, X. Dai, C.-F. Lee, Dynamics of the in sac cavitating flow for diesel spray with split injection strategy, Int. J. Engine Res. 22 (2021) 3062–3079, https://doi.org/10.1177/1468087420951330.

[3] C. Wang, A. Moro, F. Xue, X. Wu, F. Luo, The influence of eccentric needle movement on internal flow and injection characteristics of a multi-hole diesel nozzle, Int. J. Heat Mass Transf. 117 (2018) 818–834, https://doi.org/10.1016/j.ijheatmasstransfer.2017.10.057.

[4] Q. Xue, S. Som, M. Battistoni, D. Longman, H. Zhao, P. Senecal, E. Pomraning, Three-dimensional simulations of the transient internal flow in a diesel injector: effects of needle movement, in: Proceedings 25th Annual Conference on Liquid Atomization and Spray Systems (ILASS Americas), Pittsburgh, PA, USA, 2013. May.

[5] M. Battistoni, Q. Xue, S. Som, E. Pomraning, Effect of off-axis needle motion on internal nozzle and near exit flow in a multi-hole diesel injector, SAE Int. J. Fuels Lubr. 07 (2014) 167–182, https://doi.org/10.4271/2014-01-1426.

[6] C. Wang, M. Adams, T. Jin, Y. Sun, A. Röll, F. Luo, M. Gavaises, An analytical model of diesel injector's needle valve eccentric motion, Int. J. Engine Res. 23 (2022) 469–481, https://doi.org/10.1177/1468087420987367.

[7] N. Nemani, S. Preidikman, B. Balachandran, Coupled piezoelastic airfoil oscillators: nonlinear oscillations, J. Sound Vib. 618 (2025) 119226, https://doi.org/10.1016/j.jsv.2025.119226.

[8] K.Z. Wani, M. Pandey, B. Balachandran, Cantilevers attached with bluff bodies: vortex-induced vibrations, Nonlinear Dyn. 113 (2025) 30259–30278, https://doi.org/10.1007/s11071-024-10679-8.

[9] K.Z. Wani, M. Pandey, B. Balachandran, Coupled bluff body energy harvesters: vortex influenced dynamics, in: H. Yabuno, W. Lacarbonara, B. Balachandran, A. Fidlin, G. Rega, M. Kuroda, S. Maruyama (Eds.), Proceedings of the IUTAM Symposium on Nonlinear Dynamics for Design of Mechanical Systems Across Different Length/Time Scales, IUTAM Bookseries 43, Springer, Cham, 2025, pp. 355–369, https://doi.org/10.1007/978-3-031-72794-8_28.

[10] A. Bellei-Pardo, B. Balachandran, Vortex-induced vibrations based energy harvester: reduced-order modeling, system dynamics, and performance, J. Comput. Nonlinear Dyn. 21 (2026) 031003, https://doi.org/10.1115/1.4070543.

[11] C.L. Shah, D. Majumdar, C. Bose, S. Sarkar, Chordwise flexible aft-tail suppresses jet-switching by reinstating wake periodicity in a flapping foil, J. Fluid Mech. 946 (2022) A12, https://doi.org/10.1017/jfm.2022.591.

[12] C.L. Shah, D. Majumdar, C. Bose, S. Sarkar, Controlling the chaotic wake of a flapping foil by tuning its chordwise flexibility, J. Fluids Struct. 127 (2024) 104134, https://doi.org/10.1016/j.jfluidstructs.2024.104134.

[13] X. Lin, J. Wu, T. Zhang, L. Yang, Flow-mediated organization of two freely flapping swimmers, J. Fluid Mech. 912 (2021) A37, https://doi.org/10.1017/jfm.2020.1143.

[14] K. Menon, R. Mittal, Flow physics and dynamics of flow-induced pitch oscillations of an airfoil, J. Fluid Mech. 877 (2019) 582–613, https://doi.org/10.1017/jfm.2019.627.

[15] M. Boudreau, K. Gunther, G. Dumas, Free-pitching flapping-foil turbines with imposed sinusoidal heave, J. Fluids Struct. 90 (2019) 110–138, https://doi.org/10.1016/j.jfluidstructs.2019.06.012.

[16] Z. Liu, J.C.S. Lai, J. Young, F.-B. Tian, Discrete vortex method with flow separation corrections for flapping-foil power generators, AIAA J. 55 (2017) 410–418, https://doi.org/10.2514/1.J055267.

[17] G.Y. Dynnikova, Y.A. Dynnikov, S.V. Guvernyuk, Mechanism underlying Kármán vortex street breakdown preceding secondary vortex street formation, Phys. Fluids 28 (2016) 054101, https://doi.org/10.1063/1.4947449.
[18] I.K. Karathanassis, J. Hwang, P. Koukouvinis, L. Pickett, M. Gavaises, Combined visualisation of cavitation and vortical structures in a real-size optical diesel injector, Exp. Fluids 62 (2021) 7, https://doi.org/10.1007/s00348-020-03096-1.
[19] T. Cao, P. Qu, A review of cavitation phenomenon and its influence on the spray atomization in diesel injector nozzles, SAE Int. J. Commer. Veh. 17 (2024) 67–89, https://doi.org/10.4271/02-17-01-0005.
[20] T. von Kármán, Über den mechanismus des Widerstandes, den ein bewegter Körper in einer flüssigkeit erfährt [On the mechanism of resistance experienced by a body moving through a fluid], Nachr. Ges. Wiss. Göttingen Math.-Phys. Kl. 1911 (1911) 509–517.
[21] S. Taneda, Downstream development of the wakes behind cylinders, J. Phys. Soc. Jpn. 14 (1959) 843–848, https://doi.org/10.1143/JPSJ.14.843.
[22] W.W. Durgin, S.K.F. Karlsson, On the phenomenon of vortex street breakdown, J. Fluid Mech. 48 (1971) 507–527, https://doi.org/10.1017/S0022112071001721.
[23] T. Karasudani, M. Funakoshi, Evolution of a vortex street in the far wake of a cylinder, Fluid Dyn. Res. 14 (1994) 331–352, https://doi.org/10.1016/0169-5983(94)90040-X.
[24] B. Kumar, S. Mittal, On the origin of the secondary vortex street, J. Fluid Mech. 711 (2012) 641–666, https://doi.org/10.1017/jfm.2012.421.
[25] P. Vorobieff, D. Georgiev, M.S. Ingber, Onset of the second wake: dependence on the Reynolds number, Phys. Fluids 14 (2002) L53–L56, https://doi.org/10.1063/1.1486450.
[26] H. Jiang, L. Cheng, Transition to the secondary vortex street in the wake of a circular cylinder, J. Fluid Mech. 867 (2019) 691–722, https://doi.org/10.1017/jfm.2019.167.
[27] J.M. Cimbala, H.M. Nagib, A. Roshko, Large structure in the far wakes of two-dimensional bluff bodies, J. Fluid Mech. 190 (1988) 265–298, https://doi.org/10.1017/S0022112088001314.
[28] C.H.K. Williamson, A. Prasad, A new mechanism for oblique wave resonance in the 'natural' far wake, J. Fluid Mech. 256 (1993) 269–313, https://doi.org/10.1017/S0022112093002794.
[29] M.C. Thompson, A. Radi, A. Rao, J. Sheridan, K. Hourigan, Low-reynolds-number wakes of elliptical cylinders: from the circular cylinder to the normal flat plate, J. Fluid Mech. 751 (2014) 570–600, https://doi.org/10.1017/jfm.2014.314.
[30] O. Inoue, T. Yamazaki, Secondary vortex streets in two-dimensional cylinder wakes, Fluid Dyn. Res. 25 (1999) 1–18, https://doi.org/10.1016/S0169-5983(98)00027-6.
[31] R. Godoy-Diana, J.-L. Aider, J.E. Wesfreid, Transitions in the wake of a flapping foil, Phys. Rev. E 77 (2008) 016308, https://doi.org/10.1103/PhysRevE.77.016308.
[32] G.-Y. He, Q. Wang, X. Zhang, S.-G. Zhang, Numerical analysis on transitions and symmetry-breaking in the wake of a flapping foil, Acta Mech. Sin. 28 (2012) 1551–1556, https://doi.org/10.1007/s10409-012-0158-8.
[33] C.H.K. Williamson, A. Roshko, Vortex formation in the wake of an oscillating cylinder, J. Fluids Struct. 2 (1988) 355–381, https://doi.org/10.1016/S0889-9746(88)90058-8.
[34] G.Y. Dynnikova, Y.A. Dynnikov, S.V. Guvernyuk, T.V. Malakhova, Stability of a reverse Karman vortex street, Phys. Fluids 33 (2021) 024102, https://doi.org/10.1063/5.0035575.
[35] M.A. Langthjem, On the stability of a doubly infinite vortex array, Theor. Comput. Fluid Dyn. 36 (2022) 369–385, https://doi.org/10.1007/s00162-022-00604-3.
[36] C. Bose, S. Gupta, S. Sarkar, Dynamic interlinking between near- and far-field wakes behind a pitching–heaving airfoil, J. Fluid Mech. 911 (2021) A31, https://doi.org/10.1017/jfm.2020.1030.
[37] Y.A. Dynnikov, G.Y. Dynnikova, S.V. Guvernyuk, Simulation of the flexible body moving in viscous fluid, in: Proceedings of the ECCOMAS Thematic Conference on Multibody Dynamics, Barcelona, Spain, 2015, pp. 960–967.
[38] S. Moon, T. Tsujimura, Y. Gao, S. Park, J. Wang, N. Kurimoto, Y. Nishijima, M. Oguma, Biodiesel effects on transient needle motion and near-exit flow characteristics of a high-pressure diesel injector, Int. J. Engine Res. 15 (2014) 504–518, https://doi.org/10.1177/1468087413497951.
[39] X. Zhang, J. Liu, J. Wang, Effect of fuel and nozzle geometry on the off-axis oscillation of needle in diesel injectors using high-speed X-ray phase contrast imaging, J. Instrum. 11 (2016) C05015, https://doi.org/10.1088/1748-0221/11/05/C05015. –C05015.
[40] H. Jiang, L. Cheng, Strouhal–Reynolds number relationship for flow past a circular cylinder, J. Fluid Mech. 832 (2017) 170–188, https://doi.org/10.1017/jfm.2017.685.
[41] J.H. Gerrard, The mechanics of the formation region of vortices behind bluff bodies, J. Fluid Mech. 25 (1966) 401–413, https://doi.org/10.1017/S0022112066001721.
[42] H.M. Blackburn, R.D. Henderson, A study of two-dimensional flow past an oscillating cylinder, J. Fluid Mech. 385 (1999) 255–286, https://doi.org/10.1017/S0022112099004309.
[43] C.H.K. Williamson, R. Govardhan, Vortex-induced vibrations, Annu. Rev. Fluid Mech. 36 (2004) 413–455, https://doi.org/10.1146/annurev.fluid.36.050802.122128.
[44] C. Norberg, Fluctuating lift on a circular cylinder: review and new measurements, J. Fluids Struct. 17 (2003) 57–96, https://doi.org/10.1016/S0889-9746(02)00099-3.
[45] C. Liu, Y. Wang, Y. Yang, Z. Duan, New omega vortex identification method, Sci. China Phys. Mech. Astron. 59 (2016) 684711, https://doi.org/10.1007/s11433-016-0022-6.
[46] C. Liu, Y.-S. Gao, X.-R. Dong, Y.-Q. Wang, J.-M. Liu, Y.-N. Zhang, X.-S. Cai, N. Gui, Third generation of vortex identification methods: omega and Liutex/Rortex based systems, J. Hydrodyn. 31 (2019) 205–223, https://doi.org/10.1007/s42241-019-0022-4.